Behaviour and design of prefabricated connections under combined bending and compression for free-form grid structures

Guan Quan[1,2], Jun Ye[1,3], Nengbin Xu[4], Jiafeng Qi[4], Zhao Zhang[5], Hui Wu[6], Boqing Gao[1]

1. College of Civil Engineering and Architecture, Zhejiang University, Hangzhou, 310058, China
2. Department of Civil and Environmental Engineering, Brunel University London, Uxbridge, UB8 3PH, UK
3. Department of Civil and Environmental Engineering, University of Strathclyde, Glasgow, G1 1XJ, UK
4. Zhejiang Construction Engineering Group CO, LTD, Hangzhou, 310013, China
5. Urban and Rural Environment Development Centre, Inner Mongolia, 010010, China
6. Public Administration College, Zhejiang University of Finance & Economics, Hangzhou, 310018, China

Abstract

Free-form single-layer grid shells are not uncommon in long-span stadium roofs, airport terminals, exhibition pavilions, and shopping malls, the shapes of the grid surface are usually versatile to meet the architectural requirements. This emphasizes the importance of flexible joints that can adapt to various curvatures of the free-form structures. A design procedure and formulas are therefore proposed to underpin the application of a recently proposed prefabricated joint system. Three full-scale joints with different dimensions are tested under the combined bending and compression. Finite element models are proposed and validated against the tested results. The FE models provide good predictions against the test results in terms of the initial stiffness and ultimate capacities. Parametric studies are then carried out to verify the effectiveness of the proposed design formulas, as well as to investigate the influence of the key parameters on the load-carrying capacities of the proposed joints. A wider range of FE models, with a variety of combinations of bending and compression, are developed to validate the feasibility of the design formulas. The results demonstrate that the proposed design formulas can provide a reasonably good prediction of the joint strengths and deflection. The joint system can be easily designed, prefabricated off-site and easily assembled on-site, therefore has the potential to be applied in the construction of free-form shells.

Keywords: Experiments; FE analysis; Connections; Design method; Structural behaviour

1 Introduction

Space structures are widely used for large, long-span structures, such as railway stations, airport terminals, stadiums, and shopping malls [1-5]. Reticulated grid structures, like a typical space structural form, can be composed of single-layer grids, double-layer grids and triple-layer grids, according to the requirements of the space under the roof. Among them, single-layer grids have drawn much attention in recent years [6-9], due to their lightweight, as well as the "thin" and "transparent" visual impressions (Figure.1(a)). Different from multi-story buildings, grid shells usually come into the practice with a free-form surface where structural members are arranged on a highly curved surface. Therefore, they need to be properly placed and oriented concerning the carrier surface. Single-layer grid shell structures are an efficient solution to span a large space with a limited cost of construction materials, but the design of such structures needs careful consideration of overall stability and a good understanding of the connection behaviours that joint the structural members in the free-form surface with curvatures. With the applied actions over the surface, a connection will be mainly subjected to bending moment. However, when the curvature of the free-form surface is large, the connections are normally subjected to combined bending and compressive actions, as shown in Figure.1(b).

(a) Doubly curved grid shell   (b) Actions and internal forces in a connection
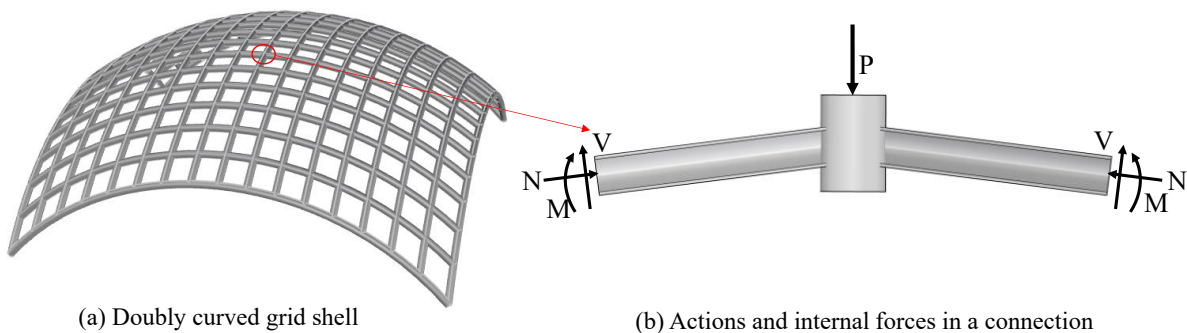
Figure 1. An example of grid shells: (a) doubly curved grid shell, and (b) actions in a connection

The research on single-layer grid structures is mainly concentrated in three areas according to the normal design procedure of space structures: Grid generation and form-finding over sophisticated free-form surfaces provided by architects [10-12]; investigation of the key parameters that affect the stability of spatial structures, including the span-to-depth ratios of space structures, the initial geometric imperfection, the strength and stiffness of connections [13, 14] and study on the mechanical behaviour

of individual joint [15-17]. Through those research, joint strength and stiffness have been found of significant importance for the analysis of load-carrying capacity and failure modes of single-layer grid structures [18-22]. Therefore, previous studies on the behaviour of joints are concentrated on the evaluation of joint ultimate capacity and stiffness. A common way to analyse space structures considering joint stiffness is to conduct experimental and/or numerical studies on the joints to obtain the load-deformation relationships and ultimate capacities. The load-deformation relationships of the joints are then incorporated in the design software of space structures, such as Robot Structure Analysis, ANSYS or MIDAS to analyse the internal forces, the joint strength will then be verified against the ultimate capacities provided in the experimental or numerical analysis.

The representative types of joints that are commonly used in space structures are Oktaplatte joint systems [23], Temcor joint system [24], MERO joint systems [25], Triodetic joint system [26] and so on. The Temcor joint system can connect I-section members. However, the members that the Temcor joint system connects are mainly aluminium alloy members. The other joint systems mentioned above allow vertical, horizontal, and twisting placement of connected members to follow the curvatures of the defined surface, but these joint systems can only connect tubular members. With the rapid development of parametric modelling and optimisation techniques in computer-aided design (CAD), the generation of grids on the complex free-form surface has become realistic [10, 27-33]. Therefore, in addition to the research on the mechanical behaviour of the joint stated above, the joint system in the single-layer grid should also be designed to have the ability to follow the curvature of the sophisticated free-form surface and to connect various section types. Ma et al. [9] proposed a new type of semi-rigid joint system for connecting I, H and rectangular cross-sectional members. Quan et al. [34] investigated the structural behaviour of a prefabricated joint subjected to uniaxial bending which can connect I-cross-sectional members. Yet, there are still limited studies that have addressed the design of joints that connect open cross-sectional members other than hollow/solid circular or rectangular sections.

In this paper, a recently proposed prefabricated joint system that can be used in the design and assembling of free-form grid structures for connecting H-section beams is proposed. Procedures and formulas are recommended for the design of the proposed joint subject to combined in-plane bending

and compressive forces. Parametric studies using finite element (FE) models, that are validated against three full-scale tests, are carried out to validate the effectiveness of the proposed design formulas, as well as to investigate the influence of the key geometric parameters. Subsequently, the proposed design formulas are validated against a wide range of FE models, with a variety of combined compressive forces and bending moments. The results indicated that the design formulas can be used to predict the strengths of the joints with reasonably good accuracy.

2 Briefing of the prefabricated joints

The proposed joint system is composed of the connected I-section beams, the front and side plates, the stiffener, the bolts, the sleeves and the central cylinder with threaded holes, as shown in Figure.2. During the assembly procedure, the bolts firstly go through the bolt holes in the front plates, and then the I-section beams will be welded with the front plate and the side plates off-site. After being transported to the site, the sleeves and the central cylinder will be assembled to the bolts. The dowels will be inserted into the holes that are shared between the bolts and the sleeves, in such, the bolts can be screwed into the central cylinder when rotating the sleeves. The advantage of the connection is that the joint can be assembled on-site and the joint could be adjusted to fit free-form surface grid shell structures by changing the relative positions between the bolt holes, and by changing the relative lengths of the top and bottom flanges of the I-sections. The detailed method to adjust the joint has been elaborated in [34]. With modern manufacturing technology, the uniqueness of each structural member and joint can be easily achieved during the manufacturing process.
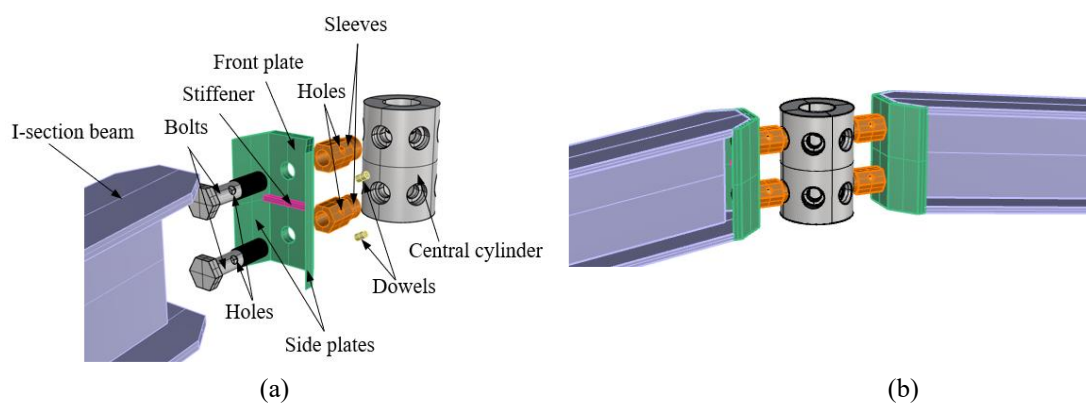

(a)   (b)

Figure 2. The configuration of the new assembled joint: (a) joint components, and (b) joint assembly

When the free-form grid structures are with large curvature, the joints will be subject to combined in-plane bending moments and compressive forces, as shown in Figure.1. In this loading condition, one bolt row is in tension or compression, depending on the ratio between the compression force and the bending moment. The sleeve at the location of the compressive bolt row is under compression. The other sleeve is free from any tensile or compressive force. The detailed force transfer routes of the joints have been introduced in detail in [34].

3 Recommended design methods of the joint

According to the geometry and the externally applied actions of the free-form grid shell structures, the internal forces of the I-section grid members and the geometries of the I-section members can be calculated and selected accordingly. In this section, when the external compression and bending moment transferred to the joint from its connected members are given, the recommended design procedures and design formulas of different components of the joint are introduced. The proposed design procedure can determine the geometries of different components of the joint using the recommended design formulas. By following the design procedure, it is expected to maximise the material utilization of different components, while ensuring the joint provides sufficient load-carrying capacity. The proposed design procedures and the design formulas of the joint components will be introduced in the following sections.

3.1 Design of the front and the side plates

The boundary conditions of the front plate, being either simply supported or clamped, are influenced by the thickness of the side plates. When designing the front plate and the side plates, the thickness of the front plate can be determined based on the equality of the internal plastic work E_{int} and the external loss of potential energy E_{ext} of the load.

$$E_{ext} = E_{int} \tag{1}$$

The external loss of potential energy is:

$$E_{ext} = F_s \Delta_s + F_b \Delta_b \tag{2}$$

5

It is reasonable to assume that the deformations of the front plate at the bolt row locations are proportional to the forces provided by the bolt or the sleeve at the corresponding locations. The deformations and the forces all refer to their absolute values. The relationship in Eq. (3 exists.

$$\Delta_b = \Delta_s |F_b/F_s| \tag{3}$$

The yield line pattern of the front plate can be drawn as shown in Figure 3, and the internal plastic work can be calculated as:

$$E_{int} = 2M_{pl,Rd}(\theta_s + \theta_b) \tag{4}$$

in which, the $M_{pl,Rd}$ is the plastic moment resistance of the front plate which is given by:

$$M_{pl,Rd} = 0.25 l_{eff} t_f^2 f_{fy} \tag{5}$$

In Eq. (5, l_{eff} is the effective yield line length; t_f is the thickness of the front plate, and f_{fy} is the yield stress of the front plate.

The relationship between the rotation angles and the bolt-row displacements can be expressed as Eq. (6.

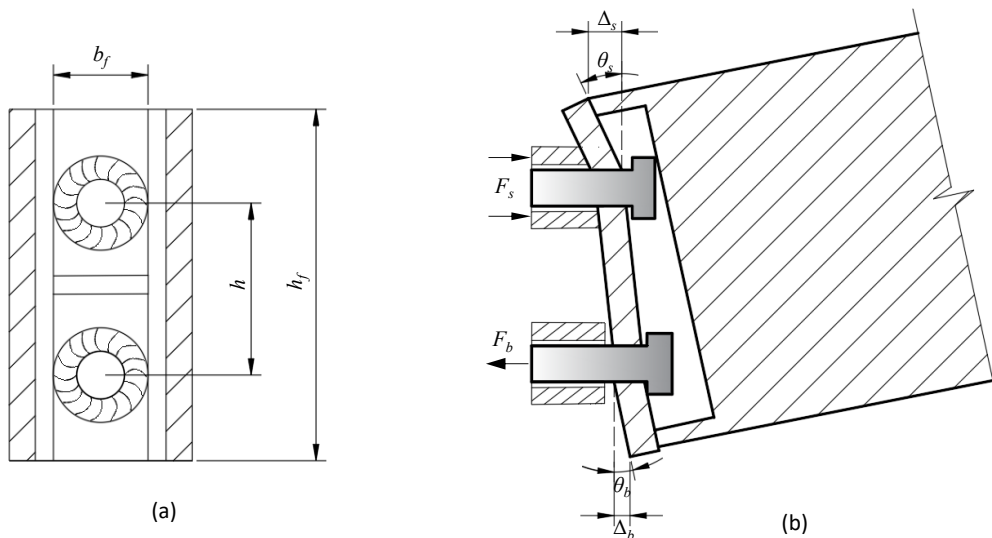$$\theta_s + \theta_b = (\Delta_s + \Delta_b)/h_{eff} \tag{6}$$

Figure 3. Yield line pattern of the front plate: (a) front view, and (b) side view

It has been observed from the tests and the FE modelling that the yield line pattern around the bolt holes is circular yielding, as shown in Figure 3 (a). Based on the design principles in Eurocode 3 [35], the effective length of the front plate l_{eff} can be calculated according to:

$$l_{eff} = 2\pi m \tag{7}$$

in which, m equals the smaller value between $h/2$ and $b_f/2$. b_f is the width of the front plate.

Substituting Eqns. (2,(3,(4,(5,(6 and (7 into Eq. (1, the thickness of the front plate is given by:

$$t_f = \sqrt{\frac{h_{eff}\,(F_s^2 + F_b^2)}{f_{fy}\pi m(F_s + |F_b|)}} \tag{8}$$

in which, F_b and F_s can be calculated according to Eq. (15 and (19, respectively. h_{eff} can be calculated according to Eq. (9 when the front plate is assumed to be simply supported at the top of the plate.

$$h_{eff} = [h_f - h - (d_b + 2) - 2T_f]/2 \tag{9}$$

in which, T_f is the thickness of the beam flanges.

To estimate h_{eff} when the front plate is assumed to be clamped at the flanges, it is assumed that the ratio of h_{eff} equals to that the deformations at the bolt-row location when the front plate is simply supported and clamped at the top and middle span of the front plate. The deformations of the bolt-row locations with the boundary conditions simply-supported and clamped can be calculated according to Eqns. (10 and (11, respectively. It is worth noting that when using Eqns. (10 and (11, it is assumed that the front plate is subject to uniformly distributed load, the restraint effects of the side plates are ignored and the boundary condition at the middle of the front plate is assumed to be identical to that of the top of the plate, being simply-supported or clamped. The deflections calculated are not accurate due to these assumptions. However, the estimations are acceptable because (1) it is impossible to derive accurate deflections at the bolt-row location, due to the complicated loading condition and boundary conditions of the front plate that are influenced by a variety of factors. The influencing factors include the location of the bolts, the forces provided by the bolt and the sleeve, the thicknesses of the front plate and the side

plates, etc. (2) The equations are to estimate the ratio of the mid-span deflections with different boundary conditions, and thus to estimate the h_{eff} when the front plate is assumed to be clamped at the top. This is to provide an estimation of the range of the thickness of the front plate according to Eq.(8. Ultimately, the estimated range will be verified by the finite element models in Section 6.1.

$$\Delta_{pin} = \frac{5F_s(\frac{h_f}{2})^3}{384EIb_f} \tag{10}$$

$$\Delta_{fix} = \frac{F_s(\frac{h_f}{2})^3}{384EIb_f} \tag{11}$$

According to Eqns. (10 and (11, h_{eff} equals to $[h_f - h - (d_b + 2) - 2T_f]/10$ when the front plate boundary condition is assumed to be clamped.

3.2 Design of the bolts and sleeves

The joint configurations are shown in Figure 4. The main geometries to determine the load-carrying capacities in this section are: the distance between the bolts h, the thicknesses of the front plate t_f and the side plates t_s, the bolt shank diameter d_b, and the diameter of the sleeve circumcircle D_s.
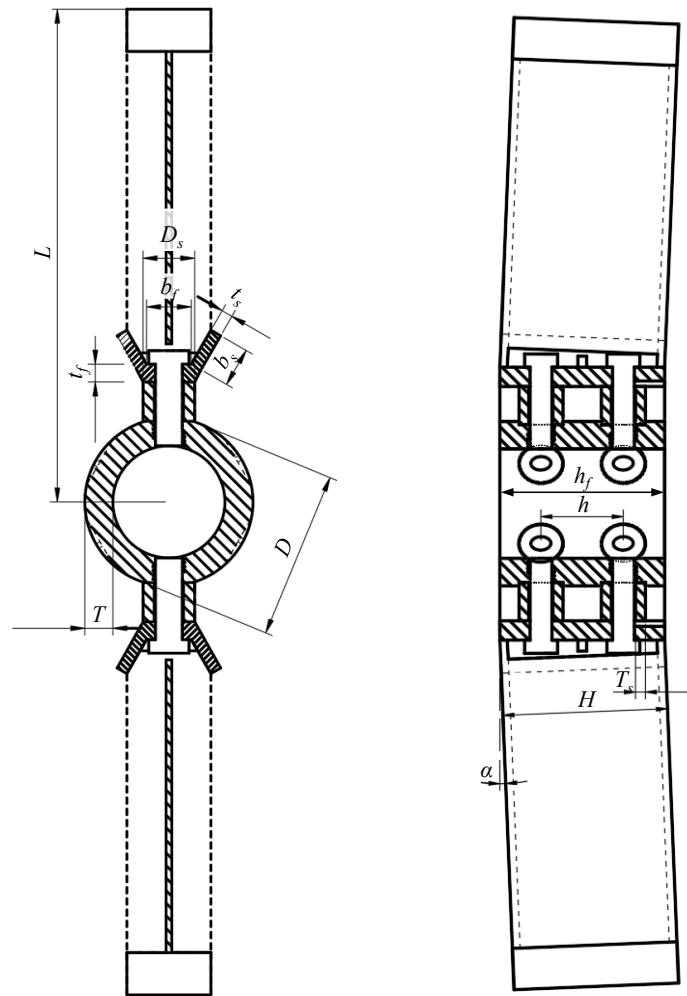
Figure 4. Configurations and dimensions of the joints

3.2.1 Distance between the bolts

It can be predicted that the in-plane flexure resistance of the joint increases with the increase of the distance between the bolts. Therefore, it is recommended to maximize the distance between the bolts, while satisfying the minimum spacing requirements recommended in Eurocode 3 [35]. The minimum edge distance of the bolts equals $1.2d_b$, where d_b is the bolt shank diameter. In the meantime, the distance between the bolts should be defined so that the contract between the sleeves and the central cylinder should be guaranteed, and the contact between the bolt head and the beam top flange should be avoided. Therefore, the maximum distance between the central points of the bolts should b calculated as:

$$h = \min(h_f - 1.2D_s, h_f - 1.2D_b - 2t_f) \tag{12}$$

in which D_s is the diameter of the circumcircle of the sleeve; D_b is the diameter of the bolt head; h is the distance between the bolts; h_f is the height of the front plate and the side plates, which equals $H/sin\alpha$ (see Figure 4), where H is the height of the I-section beam.

3.2.2 Bolt shank diameter

The tensile strength of the bolt is calculated by Eq. (13:

$$F_{t,Rd} = f_{ub}A_s \tag{13}$$

in which, $F_{t,Rd}$ is the bolt design tensile strength; A_s is the tensile stress area of the bolt. A_s can be calculated according to Eq.(14.

$$A_s = 0.7854 \times (d_b - 0.9382p)^2 \tag{14}$$

in which, p is the pitch.

According to the investigation in [34], it is reasonable to assume that when the joint is under combined compressive force and sagging moment, the bottom row is under pure compression force resisted by the sleeve or tensile force resisted by the bolt, depending on the values of the compression force and the sagging moment. The top sleeve is under compressive force. M is defined to be the bending moment transferred to the joint from the beam with a positive value when the joint is subject to a sagging moment, and N is defined to be the axial force transferred to the joint from the beam with a positive value when the joint is under compression. According to force equilibrium, the force resisted by the bottom row is given by:

$$F_b = N/2 - M/h \tag{15}$$

When F_b is a negative value, the tensile force is resisted by the bottom bolt. The design of the bolt follows the procedure in this section. The force of the bottom sleeve equals 0. When F_b is a positive value, the compressive force is resisted by the bottom sleeve. The force of the bottom bolt equals 0. The geometry of the bottom sleeve is selected to be identical to the top sleeve designed according to Section 3.2.3. This is conservative as the compressive force resisted by the bottom sleeve is always smaller than that of the top sleeve, but it is convenient for onsite installation. In the situation when both the top and

bottom sleeves are subject to compression or the design bolt diameter is less equal to 8mm, the diameter of both the top and bottom bolts are selected to be 8 mm to complete the joint installation and provide sufficient resistance redundancy to the joint.

When designing the bolt in tension, it is assumed that the bolt tensile resistance $F_{b,Rd}$ equals to the applied bolt tensile force F_b, therefore by combining Eqns. (13, (14 and (15, the minimum bottom bolt shank diameter d_b can be derived as:

$$d_b = \sqrt{\frac{(\frac{M}{h} - \frac{N}{2})}{0.7854 f_{ub}} + 0.9382p} \tag{16}$$

It is worth noting that in the FE analysis in Section 5, the bolt thread was not modelled. Therefore, the equivalent bolt shank diameter d_b' used in the FE modelling equals to:

$$d_b' = \sqrt{\frac{(4M - 2hN)}{h f_{ub} \pi}} \tag{17}$$

The top bolt is selected to be identical to the bottom bolt. After calculating the bolt diameter, the bolt distance should be updated, as it is related to the bolt diameter.

3.2.3 Sleeve geometries

The compressive strength of the sleeve can be calculated according to:

$$F_{s,Rd} = f_{us}(6 \times \sqrt{3} r_s^2 / 4 - \pi (d_b + 2)^2 / 4) \tag{18}$$

in which, $F_{s,Rd}$ is the design compressive strength of the sleeve, and f_{us} is the ultimate strength of the sleeve. To consider the installation error, the diameter of the top sleeve hole is determined to be 2 mm larger than that of the bolt shank. The sleeve cross-section of the proposed joint is a regular hexagon with the radius of its circumcircle to be r_s. The sleeve should be designed to resist the combined bending and compressive force.

Design of the top sleeve

When the joint is under compression and sagging moment, the compressive force resisted by the top sleeve can be calculated by:

$$F_s = N/2 + M/h \tag{19}$$

It is assumed that the sleeve compressive resistance $F_{s,Rd}$ equals to its applied compressive force F_s. By combining Eqns. (18 and (19, the minimum diameter of the circumcircle of the regular hexagon is derived as:

$$D_s = 2\sqrt{\frac{(2M + hN)}{3\sqrt{3}hf_{us}} + \frac{\pi(d_b + 2)^2}{6\sqrt{3}}} \tag{20}$$

Design of the bottom sleeve

When the joint bottom row is under compressive force with F_b of a positive value, the force resisted by the bottom sleeve can be calculated according to Eq. (15). By combining Eqns. (15 and (18, the minimum diameter of the circumcircle of the regular hexagon is derived as:

$$D_s = 2\sqrt{\frac{(hN - 2M)}{3\sqrt{3}hf_{us}} + \frac{\pi(d_b + 2)^2}{6\sqrt{3}}} \tag{21}$$

It can be seen by comparing Eqns. (20 and (21 that the diameter of the circumcircle of the regular hexagon of the top sleeve should be larger than that of the bottom sleeve. However, to avoid errors during the installation process, the bottom sleeve is selected to be identical to the top sleeve. The same design principle applies when the joint is under compressive force and hogging moment.

3.3 Design of the central cylinder component

To enable reliable contacts between the sleeves and the central cylinder, the central cylinder is cut to obtain a flat circular surface, facilitating the installation of bolts and sleeves. The diameter of the circular flat surface is determined to be 2 mm larger than that of the sleeve to allow manufacture and installation errors. The depth of the cut d_c should allow the installation of the sleeve as stated above. The central cylinder should be designed with sufficient thickness so that the bolts are screwed deep

enough to prevent them from pulling out. The geometry notations of the cross-section of the central cylinder are shown in Figure 5.
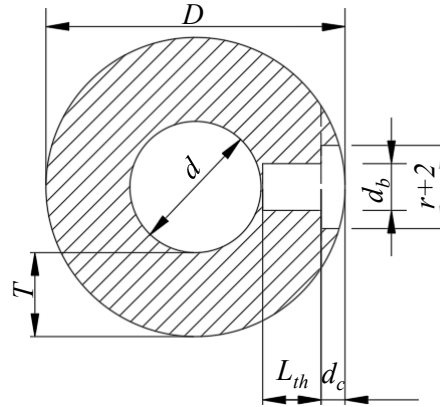

Figure 5. Notations of the cross-section of the central cylinder

The relationship between the outer diameter D and the inner diameter d of the central cylinder should also comply with the following equation:

$$D \geq d + L_{th} + d_c \tag{22}$$

in which, L_{th} is the screw depth of the bolts. According to the design guidelines for screwed ball joints in GB/T16939 [36], L_{th} should be no less than 1.1 times of the maximum bolt shank diameter that is screwed into the central cylinder. d_c is the depth needed to cut into the central cylinder to ensure that the diameter of the created flat round surface is larger than that of the sleeves. The central cylinder should also be checked against crashes between adjacent bolts when the detailed dimensions of the components have been determined.

After considering the construction constraints above, the thickness of the central cylinder is also determined to be at a minimum of 1.1 times the thickness of the front plate. The material of the central cylinder should be with higher yield stress compared with the material of the front plate. In this way, the strength of the central cylinder does not need to be checked, as it will be stronger than the front plate, and the deformation of the central cylinder can be neglected.

3.4 Estimation of the additional second-order bending moment

When the joint is under combined compressive load and sagging moment, an additional second-order bending moment will be produced and will increase as the joint deforms during the loading process. This behaviour is different from traditional beam-to-column joints in residential buildings as the axial force in beams is normally transferred together with slabs. When designing the joint, it is important to consider the additional second-order bending moment. The additional second-order bending moment can be calculated according to Eq.(23).

$$M = N \cdot w \tag{23}$$

in which, N is the axial load applied to the joint, and w is the additional lateral displacement of the joint.

The additional lateral displacement of the cylinder w is caused by the rotation of the joint, which is composed of three parts: the rotation caused by the elongation of the bolt, the rotation caused by the shortening of the sleeve and the rotation caused by the deformation of the front plate. The additional lateral displacement caused by the deformation of the I-section beam is ignored for two reasons: (i) In real design, the additional lateral displacement of the beams will be considered automatically in the full structure analysis, when estimating the applied force to the joints, and (ii) in the particular case studies presented in this paper, the beams are H150×100×6×8 with the length of 290 mm. The highest bending moment applied to the beam is 24 kN·m, which will result in a lateral deflection of 0.5 mm, calculated by Eq. (24):

$$v_{max} = ML^2/2E_b I_b \tag{24}$$

in which, M is the bending moment applied to the end of the beam; L is the length of the beam; E_b is Young's modulus, and I_b is the second moment of area of the H-section beam.

The elongation of the bolt Δ_b at fracture can be calculated by:

$$\Delta_b = \varepsilon_{ub}(l_b - L_{th}) \tag{25}$$

in which, ε_{ub} is the ultimate strain of the bolt; l_b is the length of the bolt shank, and L_{th} is the length that is screwed into the central cylinder.

The shortage of the sleeve Δ_s when it crushes can be estimated by Eq.(26):

$$\Delta_s = \varepsilon_{us} l_s \tag{26}$$

14

in which, ε_{us} is the ultimate strain of the sleeve, and l_s is the length of the sleeve.

The beam rotation θ_{bs} caused by the elongation of the bolt and the shortening of the sleeve can be calculated as:

$$\theta_{bs} = (\Delta_b + \Delta_s)/h \tag{27}$$

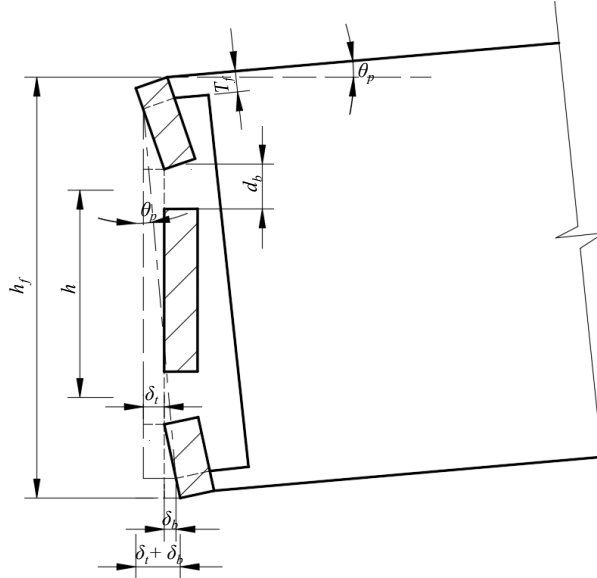The deformed shape and component notations of the front plate are shown in Figure 6.

Figure 6. The deformed shape and rotation angle of the front plate

According to the geometrical relationship shown in Figure 6, the beam rotation θ_p caused by the deformation of the front plate can be estimated according to Eq.(28):

$$\theta_p = \arcsin[(\delta_t + \delta_b)/(h_f - 2T_f)] \tag{28}$$

The largest deformation of the front plate occurs when the plate between the beam top flange and the bolt hole edge is stretched up to its ultimate strain ε_{up}. In this situation, the plate deformation δ_t caused by the compressive force transferred from the top sleeve is:

$$\delta_t = \sqrt{\{[(h_f - h - (d_b + 2) - 2T_f)/2](1 + \varepsilon_{up})\}^2 - \{[h_f - h - (d_b + 2) - 2T_f]/2\}^2} \tag{29}$$

The ratio of the deformations of the front plate at the top and bottom bolt locations is assumed to be equal to that of the forces applied to these locations. According to this assumption and Eqns. (15) and (19), the deformation of the front plate at the bottom bolt location can be calculated as:

$$\delta_b = \delta_t \times (M/h - N/2)/(N/2 + M/h) \tag{30}$$

in which, δ_b is positive when the deformation is caused by the tensile force applied by the bolt, and negative when the deformation is caused by the compressive force applied by the sleeve.

The estimated additional lateral displacement of the beam can be calculated as:

$$w = (L - D/2 - l_s)(\theta_{bs} + \theta_p) \tag{31}$$

in which, L is the length of the beam.

When designing the joint using the formula, the bolt diameter is assumed as a random value, e.g. 8 mm initially. The initial bending moment is assumed to be equal to Ne, in which e is the initial eccentricity of the loading point. The additional lateral displacement w can be estimated according to Eq. (31). The lateral displacement will then be used in the calculation of the design joint geometries introduced in Section 3.2 and the bending moment applied to the joint, which considers the second-order bending moment. An iterative process will be carried out until the real joint geometries vary within 0.1 mm in two adjacent iterations.

4 Experimental works

4.1 Test specimens and set-up

In this section, the test on three prefabricated joints subject to combined compressive forces and bending moments are introduced. The purpose of the tests is to calibrate the FE models for further parametric study. The tests were conducted using a UTM5300 Electromechanical Universal Testing Machine in the Structural Mechanics Laboratory at the College of Civil Engineering and Architecture at Zhejiang University. The configurations of the joints are shown in Figure.6, and the dimensions of the components in the joints are listed in Table 1. Compared with specimen S1, two parameters varied for specimens S2 and S3, being the thickness of the front plate, the bolt diameter, and the thickness of the side plate. The parameters of the bolts are listed in Table 2.

Table 1. Dimensions of the tested specimens

Joint group ID	I-section		Bolt	Front plate			Side plate			Bolt hole vertical distance	Central cylinder		
	Cross-section dimension (mm)	Length L (mm)		h_f	b_f	t_f	h_s	b_s	t_s	h	H	D	T
S1	H150×100×6×8	290	M20	150	50	16	150	50	10	75	150	150	30
S2	H150×100×6×8	290	M20	150	50	8	150	50	10	75	150	150	30
S3	H150×100×6×8	290	M24	150	50	16	150	50	10	75	150	150	30

Table 2. Measured dimensions of the bolts

Bolt	Shank		Sleeve		
	Diameter d_b (mm)	Length l_b (mm)	Outer diameter D_s (mm)	Inner diameter $(d_b + 2)$ (mm)	Length l_s (mm)
M20	20.0	85.5	40.0	22.0	35
M24	24.0	85.5	42.8	26.0	35

The test set-up is shown in Figure 7, where the tested joints were connected to H-section steel beams on each side of the joints. The upper and lower ends of the specimens were loaded with rollers to simulate the simply supported boundary conditions. The specimens were only allowed to rotate around their strong axis. The contacting lines between the rollers and the H-section beams deviated from the central lines of the H-section beams. When the tests started, the rollers moved downwards with the testing machine, and compressive forces were applied to the joint through the H-section beams. Bending moments of the joints were produced due to the initial eccentrical compressive loads applied to the H-section beams and additional second-order bending moments produced while the joint deformed. Linear Variable Displacement Transducers (LVDTs) were placed at the joint front plate on both sides of the central cylinder to measure the out-of-plane displacement D_v of the tested joints.
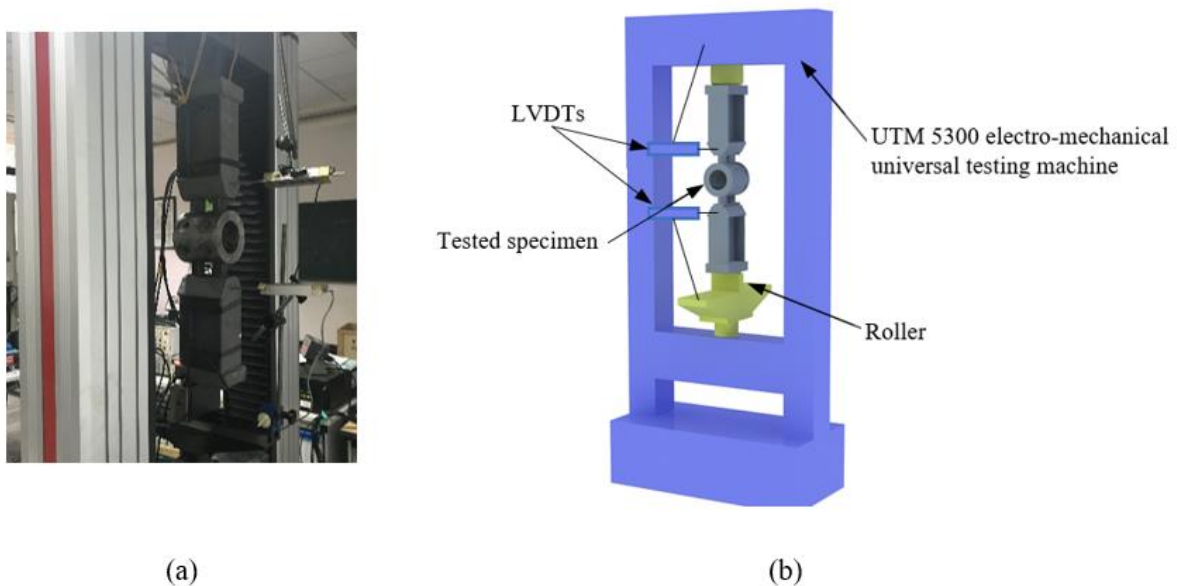

Figure 7. Test set-up: (a) test specimen and set-up, and (b) schematic drawing of the test set-up

4.2 Test procedures

The top end of the connected members was monotonically loaded at a speed of 0.5mm/min using a displacement-control loading scheme. The compressive forces were applied to the joints with an initial eccentricity of 50 mm to produce combined compressive forces and bending moments on the joints. As the specimen deformed during the test, a second-order bending moment was produced on the joint due

to the additional lateral deformation of the H-section beam. The test procedures of each specimen followed two steps: a pre-loading step and a loading step.

- In the pre-loading step, the joints were loaded until the axial load applied to the joint reached 30 kN, this produced an estimated small bending moment of 1.5 kN·m to the tested joints. The action was then unloaded from the specimens. This pre-load procedure was used to develop good contact pairs between the loading system and the specimen components, and to check whether the testing machine was working properly.

- In the subsequent loading step, the joints were then loaded after the peak capacity where the joint moment resistance started to decrease. The reasons for the decrease in joint resistances will be discussed in detail in Section 5.

4.3 Material properties

Coupon tests were conducted to obtain the material properties of the joint components. The materials were selected based on the Chinese design codes in steel structures. The test procedure followed the Chinese Mechanical Test Procedure [37]. The material of the beams and the front/side plates were grade Q345B [38] steel with a nominal yield stress of 345 MPa. The sleeves were made of grade Q235B [39] steel with a nominal yield stress of 235 MPa. The bolts were Class 10.9S [40] and the material of the central cylinder was No.45 steel [41]. The coupon test results of Q345B and Class 10.9S are summarised in Table 3. The material properties of Q235B have been tested by various researchers and were obtained from [42] with the yield stress to be 235 MPa and the ultimate stress to be 403 MPa.

Table 3. Coupon test results of Q345B and Class 10.9S

Tensile coupon designation		E (GPa)	f_y (MPa)	f_u (MPa)	ε_u (%)
Q345B	Q1	203.39	367.16	515.07	15.4
	Q2	208.83	362.99	513.98	13.6
	Q3	208.10	363.83	506.18	13.2
	Mean value	206.77	364.66	511.74	14.1
10.9S	B1	203.29	990.09	1020.26	2.1
	B2	202.60	960.07	1006.91	3.3
	B3	208.17	1003.81	1048.61	1.7
	Mean value	204.67	984.07	1025.26	2.4

4.4 Test results

The axial load-horizontal displacement curves of the three tested joints were recorded and shown in
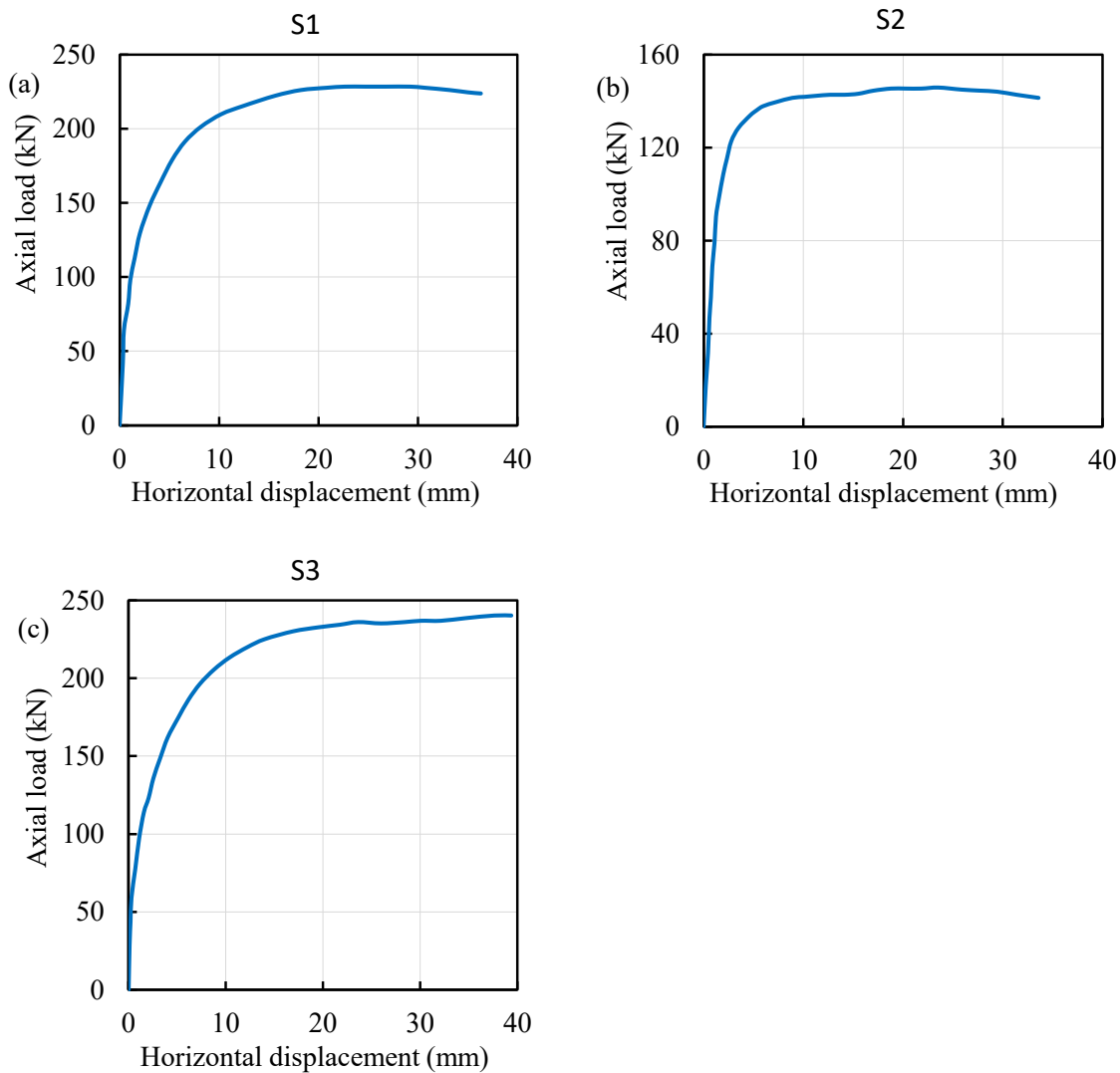

Figure 8. It can be seen that there exist initial elastic phases followed by a plastic stage until the peak point in the axial load-displacement relationships of all joints. It was observed that the crush of the sleeves of the joints S1 and S3 caused a decrease in the joint resistances after the peak points. For the joint S2, the decrease in joint resistance was caused by excessive plastic deformation of the front plate.
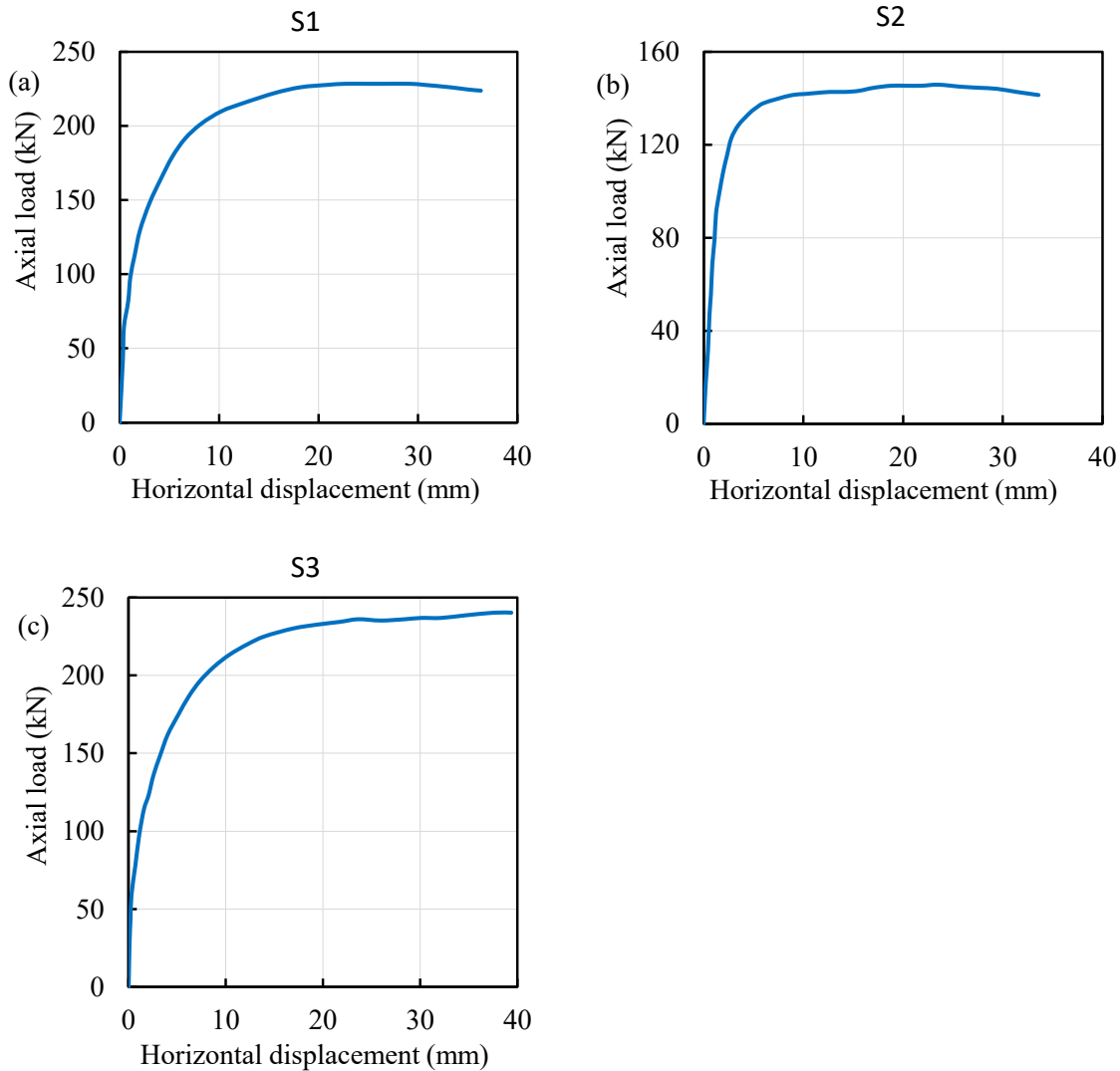
Figure 8. Comparisons of the moment-rotation curves between the tests and the FE models: (a) Joint S1; (b) Joint S2, and (c) Joint S3

5 Finite element modelling

While it is decent to have tests to calibrate Finite Element (FE) Models, tests are still expensive and time-consuming, especially for large-scale connections. It is also difficult to extract sufficient responses from each component of the joints through tests. Therefore, it is necessary to develop a reliable FE model to study the detailed behaviour of the joints, as well as to investigate the influence of the key parameters on the joint behaviour. In this section, FE models are validated against the three tests where the proposed joints are under a combined compressive force and bending moment.

5.1 Geometry, boundary conditions and mesh

The prefabricated joints tested were simulated using the commercially available FE software ABAQUS. To save computational time, only half of the joints were modelled. The geometry of the joint S1, as an example, is shown in Figure 9. The mesh and the boundary conditions are shown in Figure 10. The middle surface of the central cylinder is restrained from moving along the Y-axis, and from rotating around the X-axis and Z-axis. The beam-end "rigid block" was restrained from moving along the X-axis and Z-axis. Displacement control was applied to the beam-end "rigid block" at the location of the "purple line" to a maximum displacement of 15 mm in the Y direction. The "purple line" was 50 mm to the centre of the "rigid block", and therefore, compressive force and the moment caused by the eccentricity of the compressive force were developed in the joint. 8-node linear brick elements with reduced integration (C3D8R) [43] were employed to simulate the bolts, the plates, the beam and the solid block at the end of the beam. 4-node linear tetrahedron elements (C3D4) [43] were employed to simulate the central cylinder.

To balance result accuracy and computational efficiency, a mesh sensitivity study was carried out to obtain the mesh size of different joint components. Through the mesh sensitivity, the mesh size of 3 mm × 3 mm was appropriate to model the bolts, the sleeves, and the front and side plates. The mesh size of 10 mm × 10 mm was employed to simulate the beam and central cylinder while a mesh size of 5 mm × 5 mm was used at the bolt holes of the central cylinder. Surface-to-surface contact pairs were defined between the contacted surfaces of the model, which included the surfaces between the bolt and the sleeve, the bolt and the front plate, the sleeve and central cylinder as well as the sleeve and the front plate. The design recommendations of GB/T16939 [36] were always considered to guarantee that the bolts were not pulled out from the central cylinder. Therefore, no bolt thread was modelled, and a "Tie" interaction was defined between the bolt and the central cylinder. "Tie" interaction was also defined between the steel beam and the front plates, the steel beam and the side plates as well as between the steel beam and the "rigid block" at the end of the beam.
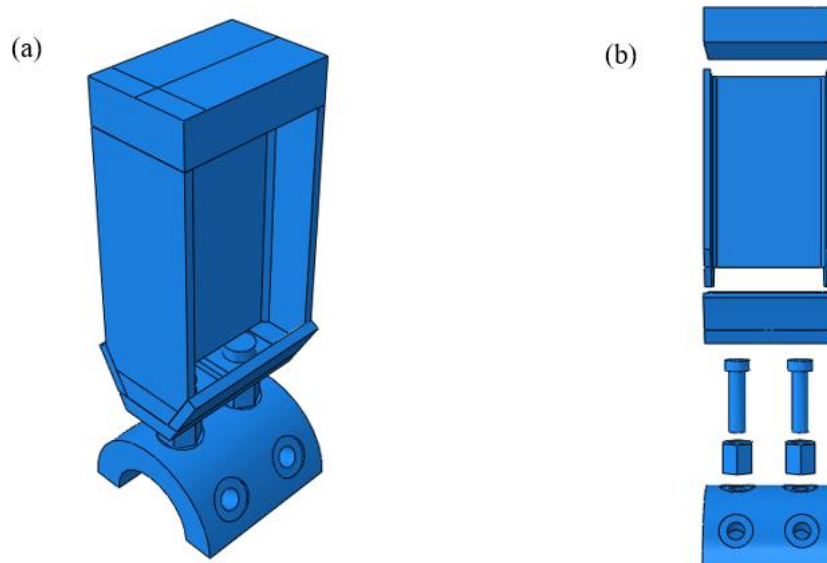
Figure 9. Geometries of the semi-rigid assembly joint (Joint S1) and its connected steel beam: (a) the
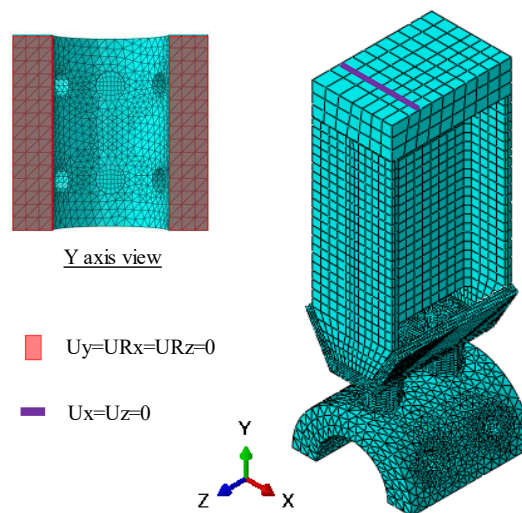
assembled model, and (b) components

Figure 10. Geometry, mesh and boundary conditions of the semi-rigid assembly joint (Joint S1)

5.2 Material properties

The material of the beams and the front/side plates are grade Q345B [44]; the material of the sleeve

is Q235B [45]; the material of the bolts is 10.9S [45], and the material of the central cylinder is No.45

[46]. For the material properties used in the FE models, the stress-strain relationship of the beams and

the front/side plates were from coupon tests introduced in Section 4.3. The stress-strain relationship of

the sleeve is from the research by Yun and Gardner [42], and the material model used for the central cylinder is from the paper [46]. The true stress-strain relationships transferred from the tested engineering stress-strain curves of steel coupon tests were taken as input for the ABAQUS modelling. A detailed explanation of the material properties has been elaborated in the paper by Guan et al. [34], and therefore the details will not be repeated here.

5.3 Comparisons of the results from the FE models against tests

FE models were developed and validated against the tests. Compared with the Joint S1, the front plate thickness of S2 was reduced from 16 mm to 8 mm, and the bolt diameter of S3 was increased from 20 mm to 24 mm. The comparisons of the axial load-displacement curves between the tests and the FE models are presented in
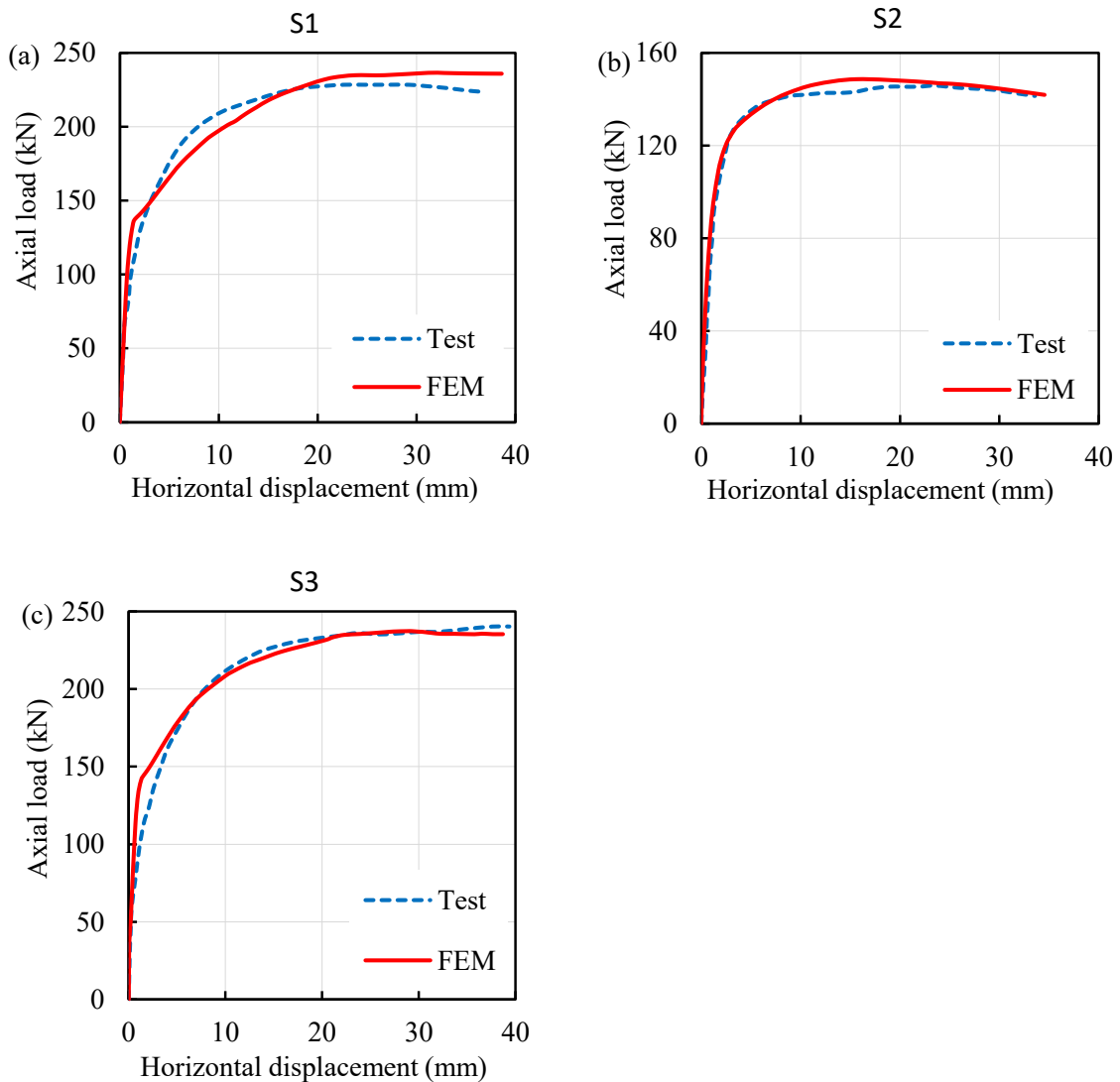
Figure 11. The displacements refer to the horizontal displacements measured by LVDTs in the tests and measured in the same places in the FE models. The axial loads and the horizontal displacements corresponding to the end of the elastic phase and the peak point are listed in Table 4. It can be observed from
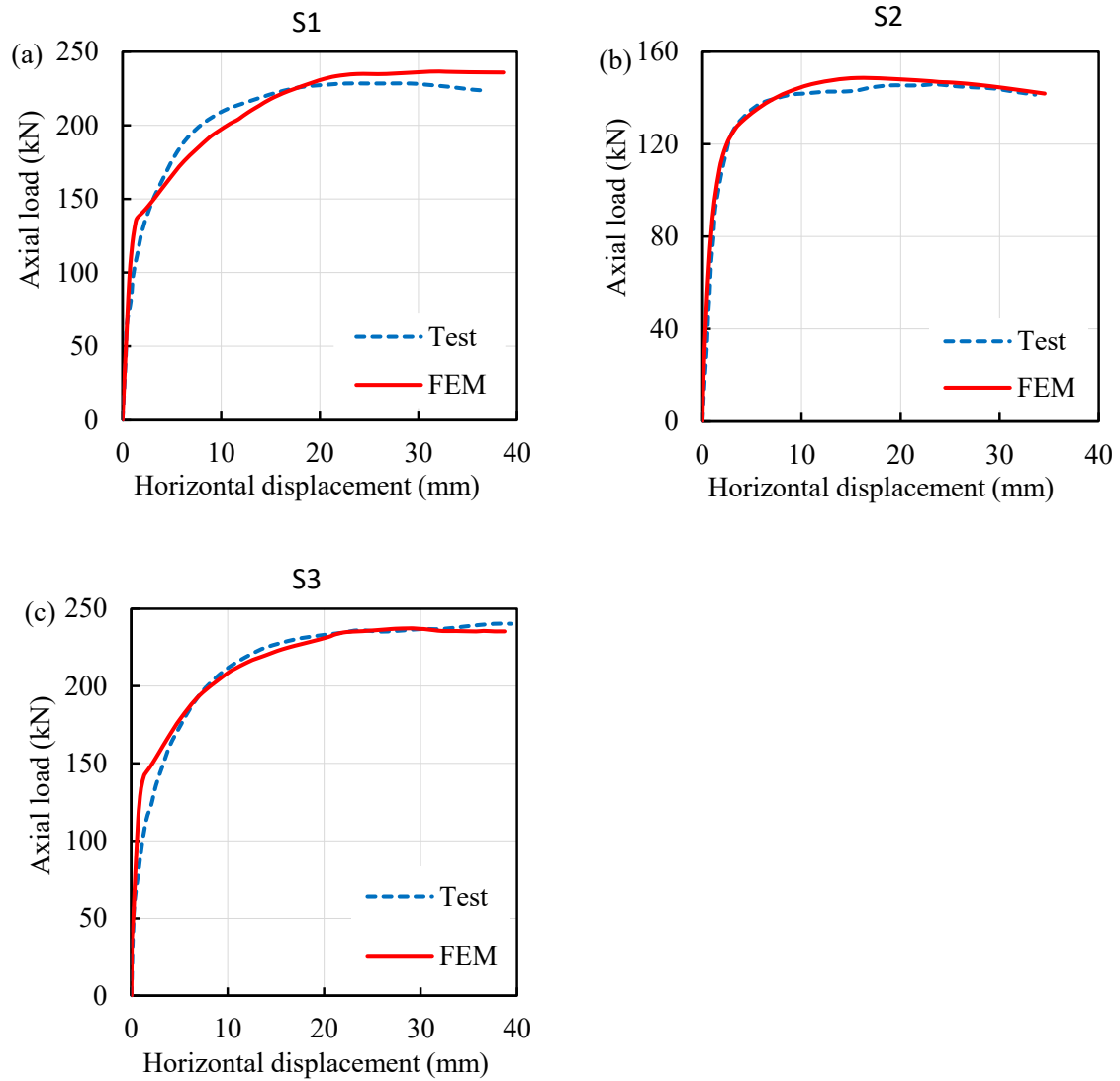

Figure 11 (a) and (c) that the elastic phases of the joints in S1 and S3 were at a higher moment compared with the results from the tests. This is possibly because the joint resistance decrease was due to the crush of the sleeves. A difference between the simplified material property model of Q235B [42]

used in the FE models and the real material properties used in the tests existed.
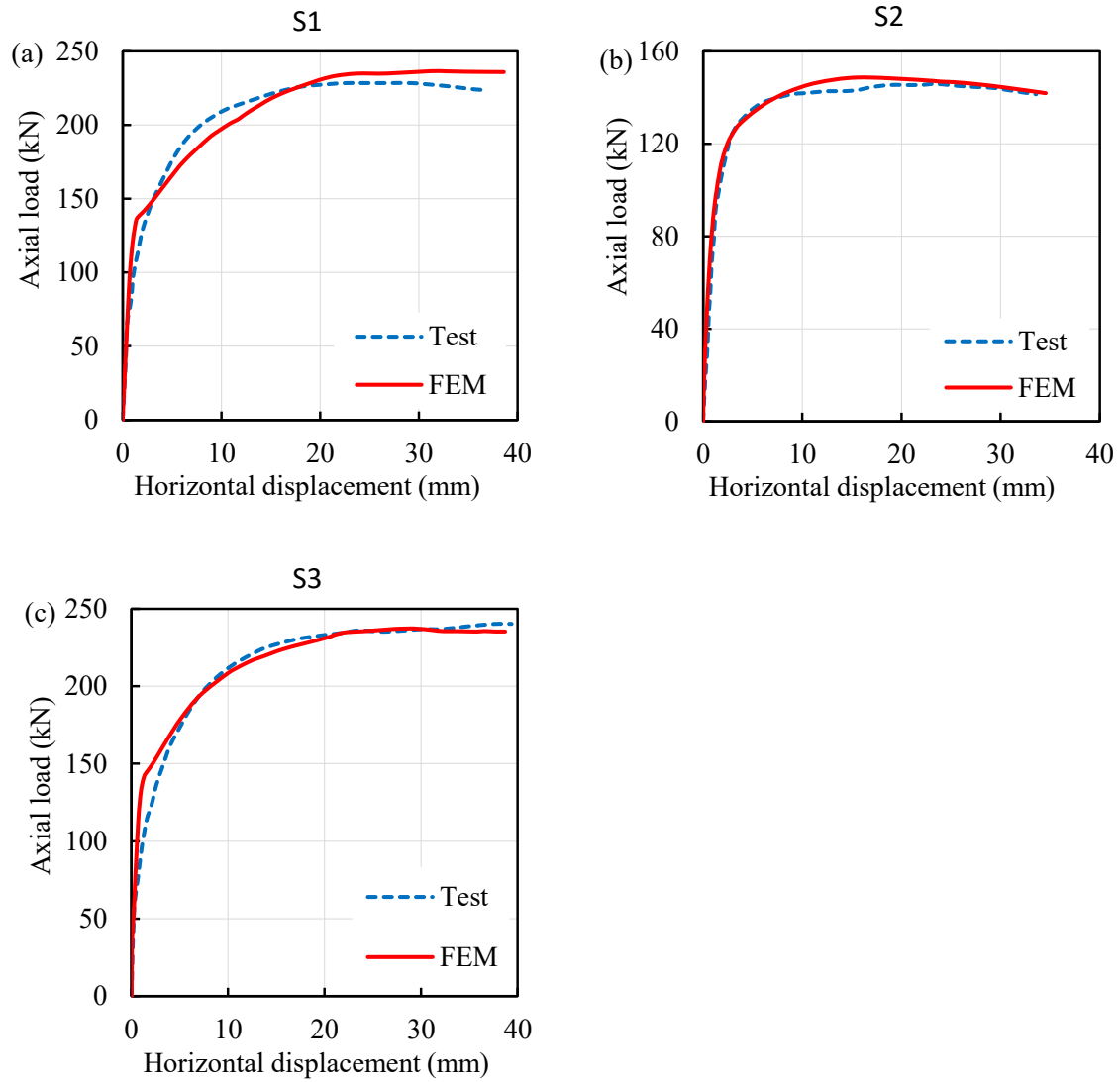

Figure 11 and Table 4 show that the results obtained from the FE analysis agree well with those from

the tests in terms of the initial elastic stiffness and the joint resistance. The deformed joints after the
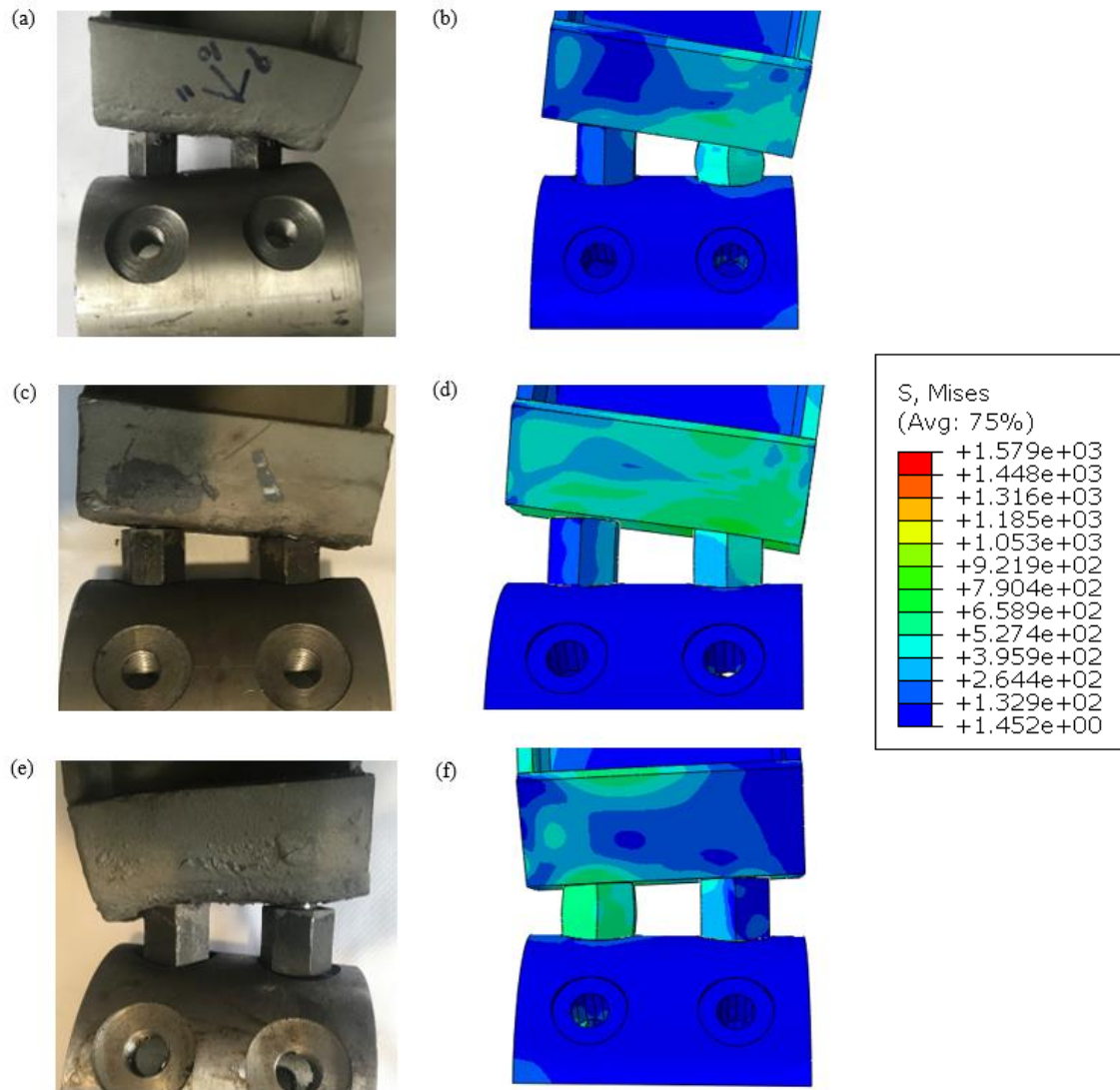
peak loads are presented in

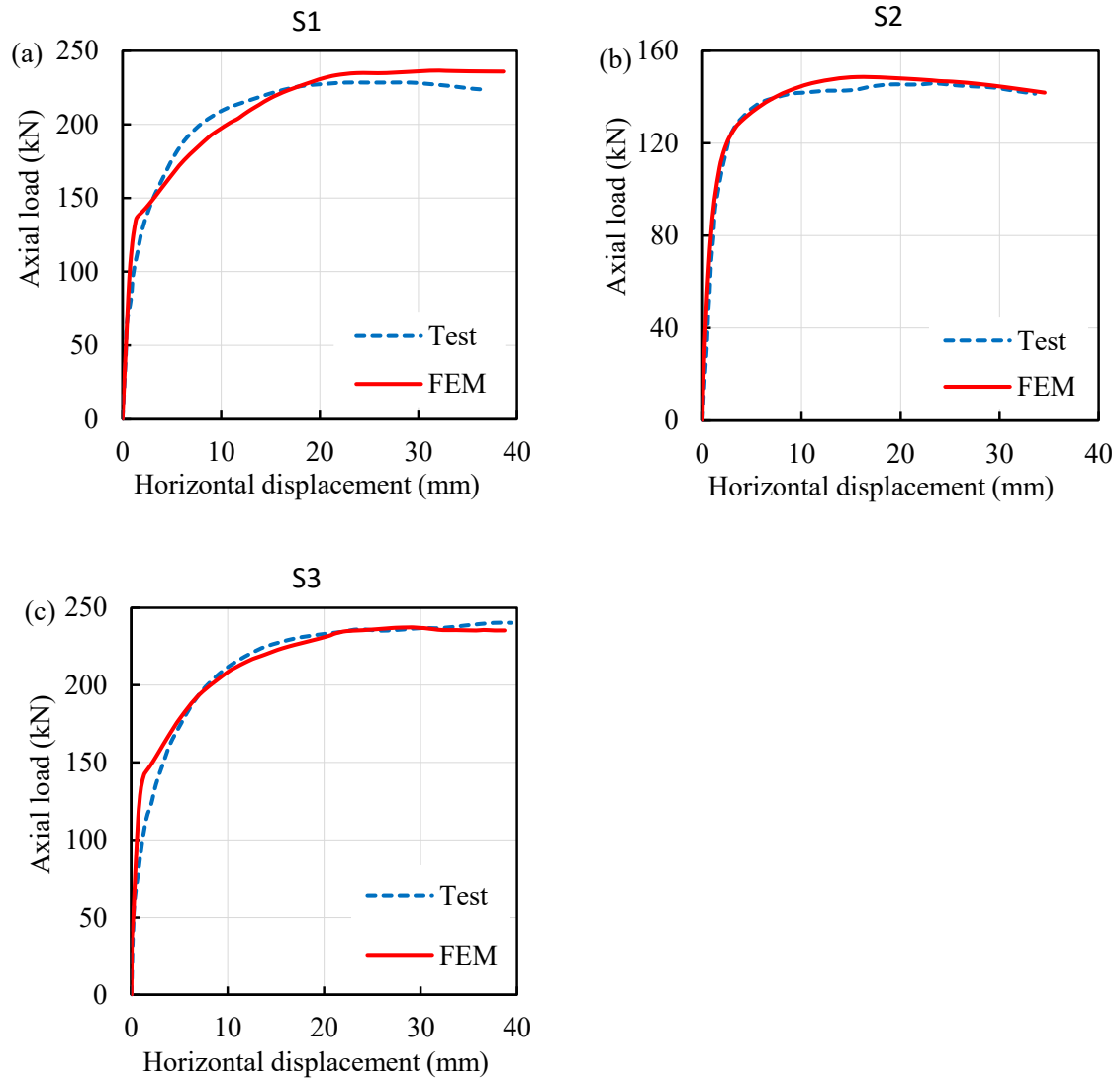Figure 12, which shows a similar deformed shape to all the test joints.

Figure 11. Comparisons of the moment-rotation curves between the tests and the FE models: (a) Joint

S1; (b) Joint S2, and (c) Joint S3

Table 4. The moments and rotations at the end of the elastic phase and at the peak point

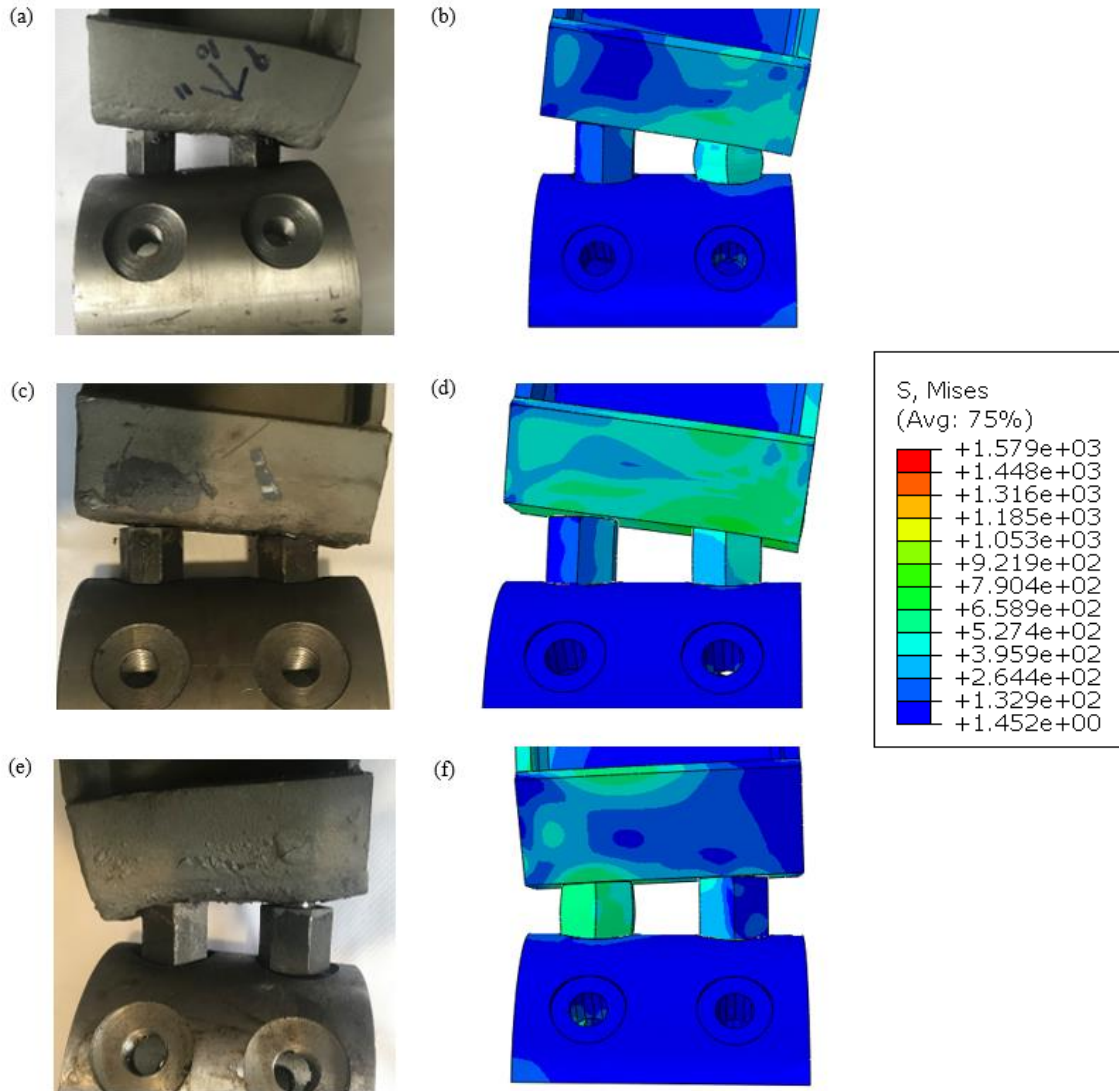| Joint group ID | End of elastic phase | | | | | | Peak point | | | | | |
| | Axial load (kN) | | | Horizontal displacement (mm) | | | Axial load (kN) | | | Horizontal displacement (mm) | | |
	Test	FEM	FEM /Test	Test	FEM	FEM /Test	Test	FEM	FEM /Test	Test	FEM	FEM /Test
S1	81.2	129.4	1.66	1.16	1.16	1.00	229.2	236.2	1.03	26.39	30.74	1.17
S2	95.4	78.2	0.82	1.16	0.87	0.75	145.0	148.8	1.03	24.94	20.01	0.81
S3	60.6	138.0	2.28	0.29	0.87	3.00	239.8	239.8	1.00	38.57	29.87	0.77

Figure 12. The deformed shape of the joints: (a) Joint S1 from test; (b) Joint S1 from FEA; (c) Joint S2 from test; (d) Joint S2 from FEA; (e) Joint S3 from the test, and (f) Joint S3 from FEA

6 Parametric study

In this section, the design formula developed in Section 3 is validated according to the recommended design procedures against numerical results. The joints discussed in this section are designed in accordance with the design procedures presented in Section 3, to resist a load combination of an initial bending moment of $M = 12$ kN·m and a compression force of $P = 240$ kN. The dimensions of the joint components calculated from the design formulas and used in the FE model are listed in Table

5. The bolt diameter, the bolt hole distance, the thickness of the front plate, the thickness of the side plates, and the diameter of the circumcircle of the sleeves are the parameters to be considered (TBC).

Table 5. Geometries of components of the joint (unit in mm)

	H-section		Bolt diameter			Front plate			Side plate		
	Cross-section	L	d_b	d_b'	h_f	b_f	t_f	h_s	b_s	t_s
FE model	H150×100×6×8	290	TBC	TBC	150	50	TBC	150	50	TBC
Formula	-	-	14.3	12.9	-	-	6.9/15.3	-	-	-

	Bolt hole distance	Central cylinder			Sleeve		
	h	H	D	T	(d_b+2)	D_s	L_s
FE model	TBC	150	150	30	22	TBC	35
Formula	98	-	-	-	16.3	41.9	-

6.1 Effects of the front plate and the side plate thickness

In this section, the thickness of the front plate (15.3 mm for simply supported boundary condition and 6.9 mm for clamped boundary condition) obtained from the formulas in Section 3 are validated against the results of the FE analysis. Recommendations are made to determine the thickness of the side plates.

The design bolt diameter and the diameter of the circumcircle of the regular-hexagon sleeve, being 15 mm and 42 mm respectively, were used in the FE models. The thickness of the central cylinder (30 mm) was selected to be above the thickness calculated from the formulas. The distance between the bolts was 75 mm.

The boundary condition of the front plate is likely to be simply supported with thin side plates for supports and is more likely to be clamped with thicker side plates. According to the formulas, the minimum thicknesses of the front plates to resist the applied load are 15.3 mm and 6.9 mm for simply supported boundary conditions and clamped boundary conditions, respectively. This means that when the thickness of the front plate is larger than or equal to 15.3 mm, the front plate can provide sufficient strength to resist the applied loads, regardless of the thickness of the side plates. When the thickness of the front plate is thinner than 6.9 mm, the joint cannot provide sufficient strength to resist the applied load, irrespective of the thickness of the side plates. When the thickness of the front plate is between 6.9

mm and 15.3 mm, the joint could possibly provide sufficient resistance, depending on the thickness of the side plates. It is worth noting that the side plates should be of sufficient thickness to provide restraints to the front plate. Therefore, the thicknesses ranging between 6 mm and 16 mm of the side plates were selected in the FE models to investigate the recommended thickness of the side plates for the design. In the FE analysis, the thickness of the front plate varied between 6 mm, 8 mm, 10 mm, 12 mm, 15.3 mm, and 16 mm. This is to verify at what thicknesses of the front plate the joint can provide sufficient strength to resist the applied axial force (240 kN for the analysed cases). For each thickness of the front plate, the thicknesses of the side plates were selected to be 4 mm, 6 mm, 10 mm, and 14 mm. This is to investigate the influence of the thickness of the side plates on the joint resistance and to propose design recommendations for the thickness of the side plates.

The axial load – horizontal displacement curves of the selected joints are shown in Figure 13. It can be seen that the joint axial load-carrying capacity increase with the increase of the thickness of the side plates. For the same thickness of the front plate, the resistances of the joints are very close when the thicknesses of the side plates are 10 mm and 14 mm. This indicates that the restraint effect of the side plates makes small difference to the resistance of the joints when the thickness of the side plates reaches 10 mm for the analysed cases. When the thicknesses of the front plates are 6 mm and 8 mm, the maximum axial load resistances of the joints are 150 kN and 200 kN, respectively, when the thickness of the side plates is 14 mm. This is below the design axial load of 240 kN. While according to the formula prediction, the joint load-carrying capacity should be above 240 kN when the thickness of the front plate is not less than 6.6 mm with clamped boundaries. This indicates that an ideal clamped boundary condition cannot be achieved even when the thickness of the side plates is as thick as 14 mm. When the thicknesses of the front plates are 10 mm, and 12 mm, the axial load resistances of the joints could be below or above 240 kN, depending on the thicknesses of the side plates. When the thickness of the front plate is 10 mm, the side plates are required to be 14 mm to enable the resistance of the joint to exceed the design load. When the thickness of the front plate is 15.3 mm, which equals the design thickness of the front plate, the axial load resistances of the joints are all above the design load of 240 kN even with the thinnest side plates of 4 mm thick. When the thickness of the front plate is 16 mm,

the axial load resistances of the joint are all above 240 kN, irrespective of the thicknesses of the side plates. The FE results are consistent with the prediction from the formulas proposed in Section 3.
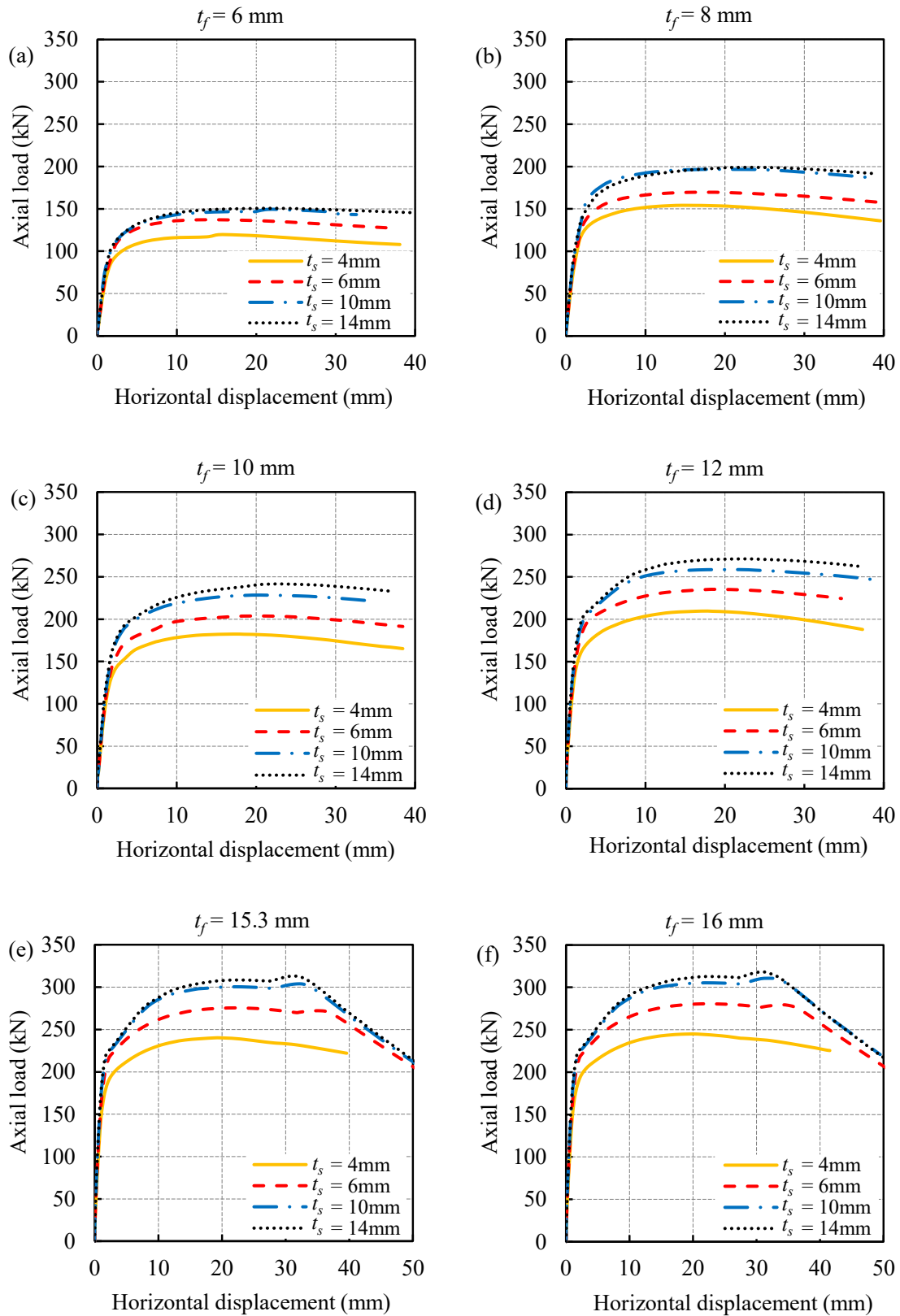
Figure 13. Axial load – horizontal displacement curves of the selected joints: (a) t_f = 6 mm; (b) t_f = 8 mm; (c) t_f = 10 mm; (d) t_f = 12 mm; (e) t_f = 15.3 mm, and (f) t_f = 16 mm

Figure 14 presents the deformed shape of the joints at the peak point via Von Mises stress contours. The red contours of 595 MPa and 1041 MPa are the ultimate strengths of the front plate and the bolt, respectively, when transferring the engineering stress of 511.74 MPa and 984 MPa to the true stress. Representative thicknesses of the front plate of 6 mm, 15.3 mm and 16 mm are presented. For each thickness, two extreme cases, being the side plate thicknesses of 4 mm and 14 mm, are presented at the peak point. It can be observed from Figure 14 that when the thickness of the front plate equals 6 mm, the decrease of the joint resistance is caused by the excessive plastic and out-of-plane deformation of the front plate at the location between the top flange of the beam and the top bolt. When the thicknesses of the front plates are equal to 15.3 and 16 mm, and the thickness of the side plates equals 4 mm, the decreases in the joint resistances are caused by the out-of-plane deformation of the side plates at the location close to the top bolts. When the thicknesses of the front plates are equal to 15.3 and 16 mm, and the thickness of the side plates equals 14 mm, the decreases in the joint resistances are caused by the simultaneous crush of the top sleeves and necking of the bottom bolts.
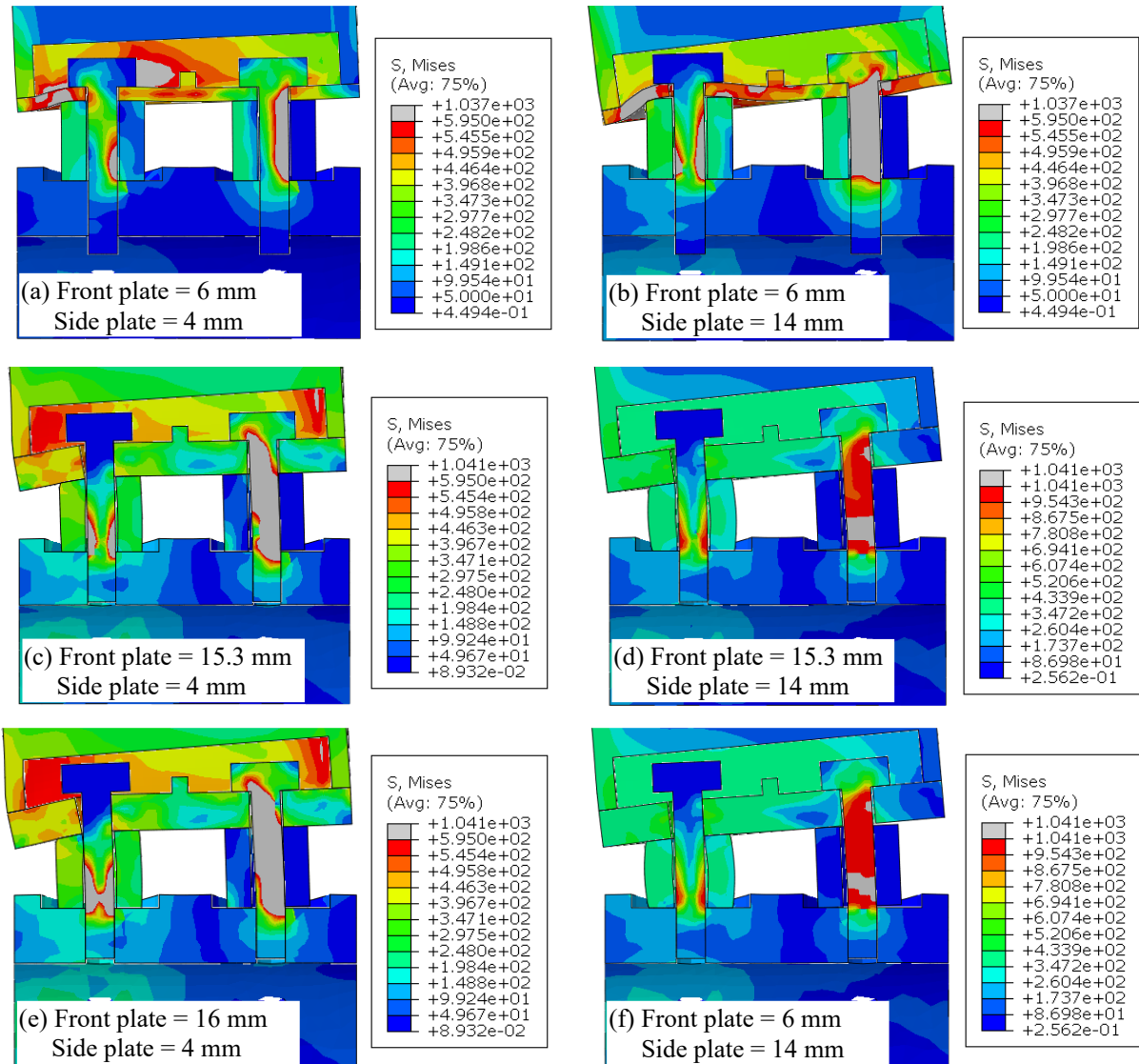
Figure 14. Von Mises stress contour of joints with various dimensions of the front plate and side plate

thicknesses

According to the analysis and observations above, it is concluded that the design formulas in Section 3 can provide a reasonably good prediction of the design thickness of the front plate. It is recommended to use the simply-supported boundary condition for the design of front plate thickness. It is recommended to select half of the thickness of the front plate as the design thickness for the side plates to provide a reasonable yet conservative joint resistance.

6.2 Effect of the distance between the bolts

In this section, the effect of the distance between the bolts on the joint load-carrying capacity is discussed. This is because, during the FE analysis, it was found that the bolt distance has an effect on

the joint load-carrying capacities when designing in accordance with the proposed formulas. For the loading condition with the axial force N of 240 kN and initial bending moment M of 12 kN, the joints were designed with different distances between the bolts. Other geometric parameters of the joints were calculated according to the defined distance between the bolts. According to the formulas in Section 3.2.1, the maximum distance between the bolts is 98 mm. In the analysis, the distances between the bolts were selected to be 60 mm, 75 mm and 90 mm. The connected H-section beams remained to be 290 mm long. The thicknesses of the central cylinder remained to be 30 mm. The other design component geometries corresponding to the selected bolt distances are listed in Table 6.

Table 6. List of designed component geometries in the case studies (in mm)

Bolt hole distance	Bolt diameter		Sleeve			Front plate			Side plates		
h	d_b	d_b'	(d_b+2)	D_s	L_s	h_f	b_f	t_f	h_s	b_s	t_s
60	18.7	17.3	20.7	48.5				19.3			9.7
75	14.3	12.9	16.3	41.9	35	150	50	15.3	150	50	7.6
90	10.7	9.3	12.7	36.0				12.1			6.1

The axial load – horizontal displacement curves of the analysed joints with different bolt distances are shown in Figure 15. It can be seen that when the bolt distance equals 60 mm, the maximum axial resistance occurs when the horizontal displacement equals 23 mm. It can be observed from the FE model that at this point, the crush of the top sleeve occurs. When the horizontal displacement equals 39 mm, there is a short increase in the axial resistance of the joint before the joint resistance decrease again. This occurs because the sleeve deforms excessively, which accelerates the increase of the tensile stress of the bottom bolt before necking occurs. When the bolt distances are equal to 75 mm and 90 mm, a similar tendency occurs in the axial load-horizontal displacement curves. However, the peak points occur when the necking of the bottom bolts takes place at the horizontal displacements of 34 mm. This is because in these two cases, the top sleeves do not crush before the necking of the bottom bolts. It can be seen that the axial load-carrying capacities of the joints decrease with the increase of the distance between the bolts even when all the three joints are designed according to the design formulas. Possible reasons are investigated by inspecting the Von Mises stress contour with the deformed shape of the three models at the points when the necking of the bottom bolts starts, as shown in Figure 16. 403 MPa is the ultimate strength of the sleeves.
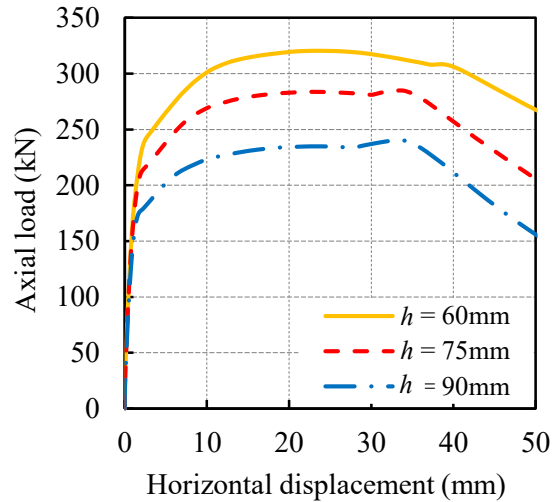
Figure 15. Axial load – horizontal displacement curves of the selected joints with different bolt distances

It can be seen that when the bolt distance equals 60 mm, the thickness of the front plate is thick (19.3 mm) and the deformation of the front plate is small. The sleeves are close to each other. Due to displacement coordination, the top sleeve and a part of the bottom sleeve are under compression. When the bolt distance equals 90 mm, the thickness of the front plate is thin (12.1 mm) and the deformation of the front plate is concentrated around the top sleeve. The sleeves are far from each other. Only the top sleeve is under compression. Therefore, when the bolt distance equals 60 mm, the axial load-carrying capacity of the joint is provided by both the top sleeve and a part of the bottom sleeve of the joint, which is higher than that of the joint when the bolt distance equals 90 mm and the axial load-carrying capacity of the joint is solely provided by the top sleeve. For the case when the bolt distance equals 75 mm, the situation is in between the two cases when the bolt distances are equal to 60 mm and 90 mm. The case when the bolt distance equals 90 mm reflects the assumption that the compression is solely resisted by the top sleeve when designing the joints in accordance with the formulas. The axial load-carrying capacity of the joint is 242 kN, which is close to the design axial load of 240 kN. In order to provide a reasonable safety margin for the design joint, it is recommended to define the bolt distance to be half of the high of the front plate h_f.
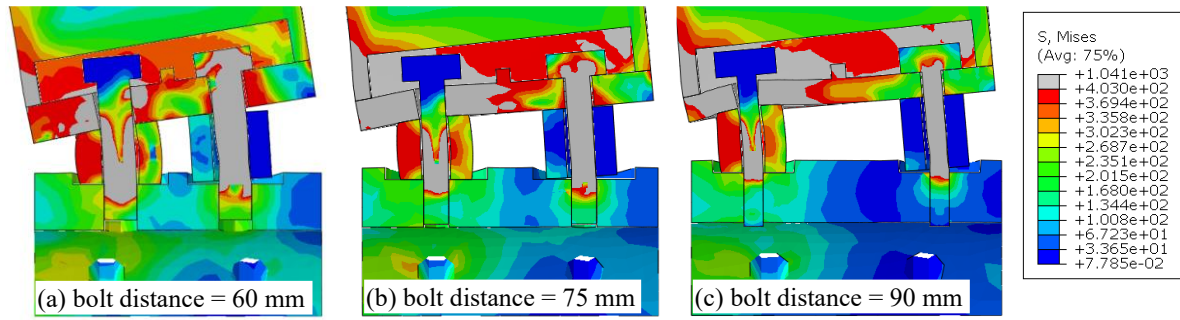
Figure 16. Von Mises stress contour of joints with variety of bolt distances: (a) h = 60 mm; (b) h = 75 mm, and h = 90 mm

6.3 Effect of the sleeve dimensions

In this section, the diameter of the circumcircle of the sleeves calculated from the proposed formulae in Section 3.2 is validated against the results of the FE analysis. Parametric studies of the sleeve dimensions on the load-carrying capacity of the joints are also conducted. According to the proposed recommendations in Section 6.1, the thickness of the front plate was set to be 15.3 mm, and the thickness of the side plates was determined to be 7.6 mm in all parametric studies in this section to provide a suitable second-order bending moment to the bolts and the sleeves. The modelled diameter of the bolts d_b' was taken as 12.9 mm. According to the formulas, the joint load-carrying capacity should exceed the design value of 240 kN when the diameter of the circumcircle of the sleeves is no smaller than the design thickness of 41.9 mm. The thickness of the central cylinders was designed to be 30 mm as calculated from the formulas. The distance between the bolts was set to be 75 mm according to the recommendation in Section 6.2. The diameter of the circumcircle of the sleeves varied from 38 mm to 50 mm to investigate the influence of the sleeve area on the load-carrying capacity of the joints.
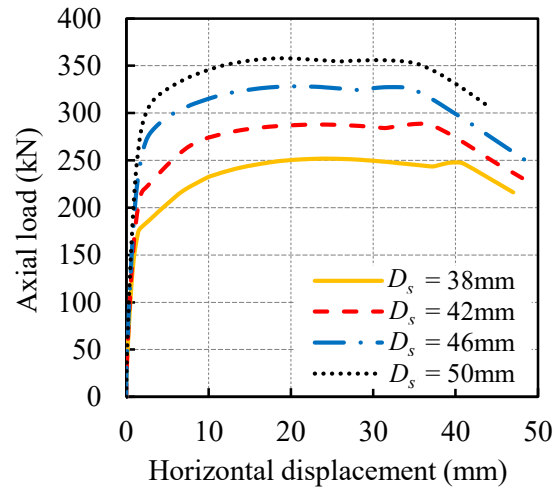
Figure 17. Axial load – horizontal displacement curves of the joint with different diameters of the circumcircles of the sleeves

It can be seen from Figure 17 that the axial load-carrying capacities of the joints increase with the increase of the diameters of the circumcircles of the sleeves. When the diameters of the circumcircles of the sleeves equal 41.9 mm, the joint load carrying capacity is 287.8 kN, which is higher than the design load of 240 kN by 19%. This is acceptable as the proposed design method provides a reasonable conservative solution.

The Von Mises stress contours at the peak points are shown in Figure 18. It was observed that the decrease of the load-carrying capacities of the joints is all caused by bolt necking. For the joint with the diameter of the circumcircles of the sleeves to be 38 mm, the crush of the top sleeve was observed before the necking phenomenon of the bottom bolt. This causes the first peak point on the axial load-horizontal displacement curve when the horizontal displacement equals 24.5 mm. After crush, the deformation of the top sleeve increases rapidly and transfers the forces to the bottom bolt, in such accelerating the bolt necking. For this case, the Von Mises stress contour at the second peak point is shown. For other joints, the crushes of the sleeves were not observed. This is because the areas of the sleeves are large, and the necking of the bolts occurs before the crush of the sleeves.
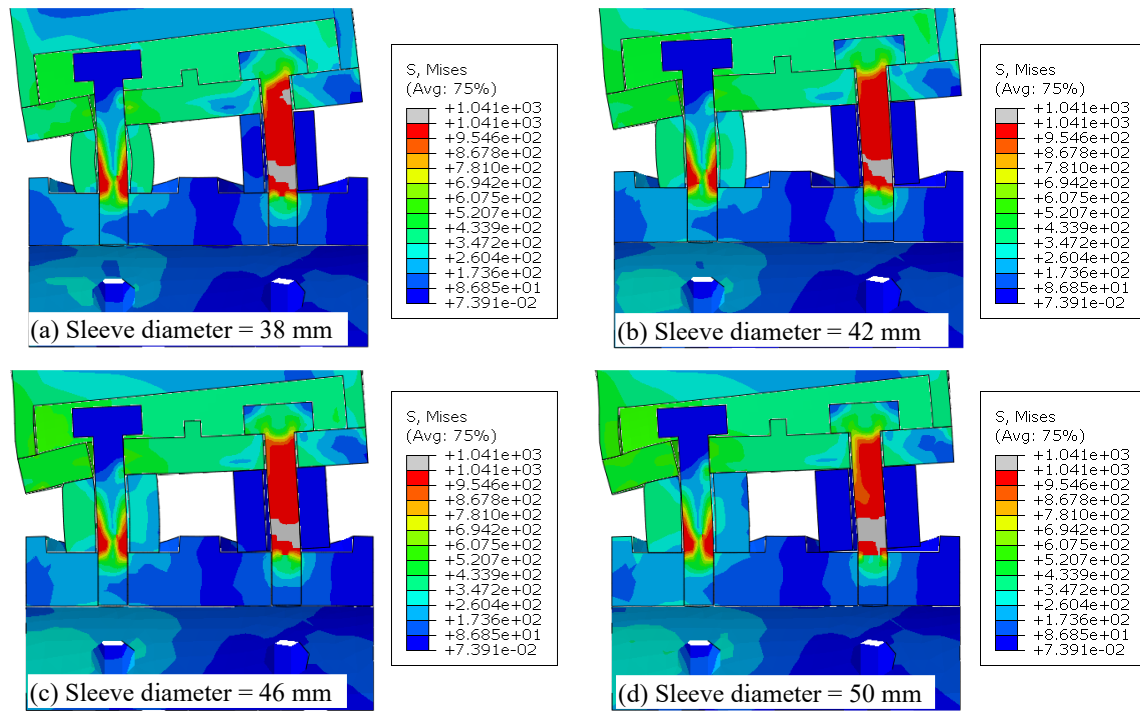
Figure 18. Von Mises stress contour of joints: (a) D_s= 38 mm; (b) D_s = 42 mm; (c) D_s =46 mm, and (d) D_s = 50 mm

6.4 Effect of bolt diameters

In this section, the effect of bolt diameter is investigated through both the formulas in Section 3.2 and the results of the FE analysis. It is worth noting that the bolt shanks modelled in the FE analysis were the equivalent bolt shank diameters d'_b as stated in Section 3.2.2. According to the recommendations in Sections 6.1 to 6.3, the thickness of the front plate was determined to be 15.3 mm; the thickness of the side plates was determined to be 7.6 mm, and the diameter of the circumcircle of the sleeves is 41.9 mm. The distance between the bolts was 75 mm. The 30 mm thickness of the central cylinder was selected to provide sufficient strength to the joints. As the design bolt diameter d_b is 14.3 mm, the bolt diameters varied from 8 mm to 20 mm to investigate the influence of the bolt diameters on the joint capacities. To keep the areas of the sleeves identical for all the design cases, the inner diameters of the sleeves were 2 mm larger than the bolts, and the diameters of the circumcircles of the sleeves were calculated to be 39.4 mm for an 8 mm bolt (d'_b= 6.6 mm), 40.2 mm for 12 mm bolt (d'_b=10.6 mm), 42.0 mm for 16 mm bolt (d'_b= 14.6 mm), and 44.3 mm for 20 mm bolt (d'_b= 18.6 mm).
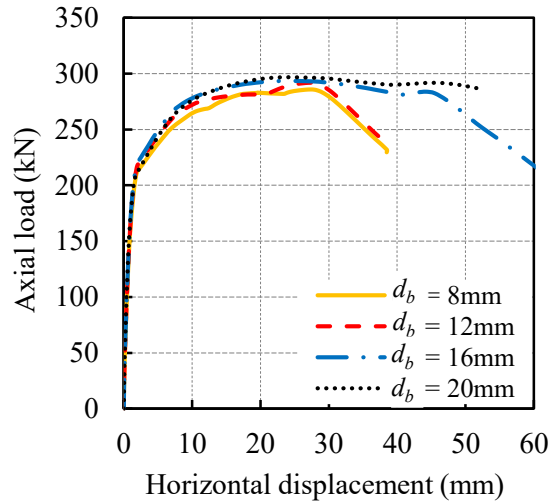
Figure 19. Axial load – horizontal displacement curves of the joint with different bolt diameters

It can be seen from Figure 19 that the axial load-carrying capacities of the joints increase slightly with the increase of the bolt diameters, and are all above 240 kN. This is because as the bolts and the sleeves work in pairs within the joints, the variation of the bolt diameters does not significantly change the overall resistance of the summation of the bottom bolts and the top sleeves.

The deformed shape with Von Mises stress contours of the relevant joints at the peak points is shown in Figure 20. It can be seen that when the bolt diameters are equal to 8 mm and 12 mm, the decrease in the joint resistances is caused by the necking of the bolts. When the bolt diameter equals 16 mm, the decrease of the joint load-carrying capacity is dominated by the crush of the sleeve. As the bolt diameter is slightly larger than the design bolt diameter (14.3 mm), the excessive deformation of the top sleeve subsequently causes the necking of the bottom bolt. When the bolt diameter equals 20 mm, the decrease of the joint load-carrying capacity is dominated by the crush of the sleeve. As the bolt diameter is much larger than the design bolt diameter, the necking of the bottom bolt does not occur when the top sleeve has been crushed significantly.
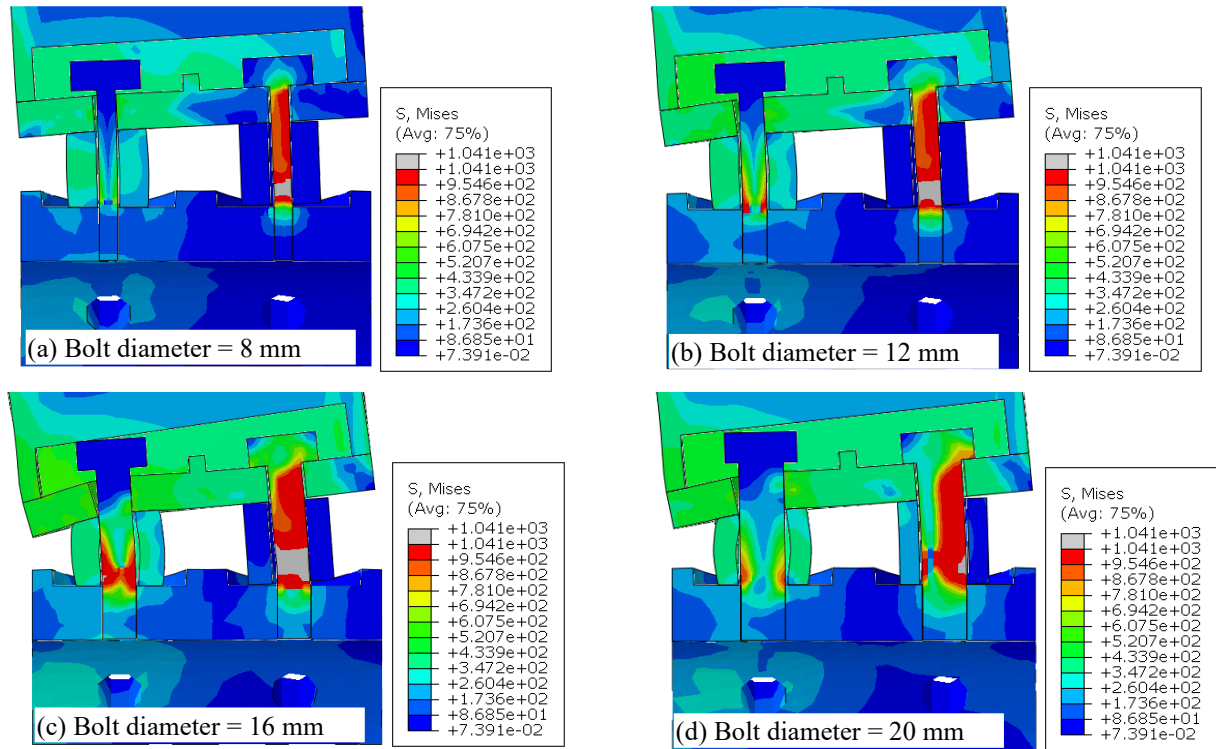
Figure 20. Von Mises stress contour of joints at peak points: (a) d_b = 8 mm; (b) d_b = 12 mm; (c) d_b = 16 mm, and (d) d_b = 20 mm

7 Verification of the design formulas

In this section, case studies are carried out to verify the joint strength predicted from the design formulas and procedures in section 3 in a wider range. Two compressive forces of 400 kN and 200 kN were applied to the joints. The initial eccentricities of the compressive force were 20 mm, 40 mm, and 60 mm, which produced the initial applied bending moments M. The component geometries designed according to the recommended formulas for all the cases are listed in Table 7.

Table 7. List of designed component geometries in the case studies (in mm)

	Loading	H-section					Front plate		Side plate		
		Cross-section	L	h_f	b_f	t_f		h_s	b_s	t_s	
Case 1	N = 400 kN M = 24 kN·m	H150×100×6×8	290	150	50	19.0		150	50	9.5	
Case 2	N = 400 kN M = 16 kN·m	H150×100×6×8	290	150	50	18.6		150	50	9.3	

Case 3	N = 400 kN M = 8 kN·m	H150×100×6×9	290	150	50	18.6	150	50	9.3
Case 4	N = 200 kN M = 12 kN·m	H150×100×6×10	290	150	50	14.5	150	50	7.3
Case 5	N = 200 kN M = 8 kN·m	H150×100×6×11	290	150	50	13.9	150	50	7.0
Case 6	N = 200 kN M = 4 kN·m	H150×100×6×12	290	150	50	13.4	150	50	6.7

	Bolt diameter		Bolt hole distance	Central cylinder			Sleeve		
	d_b	d_b'	h	H	D	T	(d_b+2)	D_s	L_s
Case 1	19.5	18.1	75	150	150	28	19.4	55.1	35
Case 2	15.5	14.1	75	150	150	24	17.5	50.2	35
Case 3	9.7	8.3	75	150	150	17	11.7	43.7	35
Case 4	14.5	13.1	75	150	150	22	16.5	40.3	35
Case 5	11.7	10.3	75	150	150	19	13.7	36.4	35
Case 6	8.0	6.6	75	150	150	15	10	31.7	35

The comparisons between the results of the finite element analysis (FEA) for each case and the predicted axial load-carrying capacities of the joints with red solid lines are shown in Figure 21. The comparisons of the axial load-carrying capacities, moment resistance and the joint displacement at peak points between the FE models and the formula predictions are listed in Table 8. It is worth noting that for Cases 3 and 5 in which their existing two peak points, the joint resistance at the second peak point is recorded as the joint maintains good resistance between the first and second peak points. It can be seen from Table 8 that the design formulas can provide reasonably good yet conservative predictions that agree with the FE results in terms of the axial load-carrying capacities and the moment resistances for all the validated cases. The predicted joint displacements at the peak points are of acceptable accuracy compared with the FE modelling results.

It is worth noting that in Eurocode 3 [36] the yield stress rather than the ultimate tensile strength is often used when designing a component under compression actions. Based on the same philosophy, it is arguable that when designing the sleeves, the yield stress (f_{ys}) of the sleeves may also be used in Eqns. (18, (20 and (21 to calculate the resistance of the sleeves. In order to assess the feasibility of using the

yield stress in the design formulas of the sleeves, the design resistances of the joints are calculated and shown with dashed lines in Figure 21. The joint resistances were calculated by assuming that the geometry of the sleeves calculated from the given design loads remained unchanged, and replacing the ultimate strength (f_{us}) of the sleeves by the yield stress (f_{ys}) of the sleeves in Eq.(18. In all the cases, the sleeves were the most onerous component, which governed the resistance of the joints. It can be observed from Figure 21 that the design resistances of the joints are up to 40% less than the design load, which also equals the ratio between the yield stress and the ultimate strength of the sleeves. The design formulas will provide more conservative results if the yield stress of the sleeves is used in the design, however, without the use of strain hardening in the elastic-to-plastic stage, the deformation of the joint can be better controlled.

Table 8. Result comparisons between the FE models and the formula predictions

| Case ID	Axial load-carrying capacity (kN)			Moment resistance (kN·m)			Displacement at peak point (mm)		
	FEM	Formula	FEM/Formula	FEM	Formula	FEM/Formula	FEM	Formula	FEM/Formula
Case 1	423.7	400.0	1.1	36.4	35.0	1.0	30.9	27.6	1.1
Case 2	430.9	400.0	1.1	28.9	27.2	1.1	34.7	28.0	1.2
Case 3	467.8	400.0	1.2	22.0	19.2	1.1	26.4	27.9	0.9
Case 4	230.5	200.0	1.2	19.3	18.0	1.1	28.3	30.0	0.9
Case 5	243.5	200.0	1.2	14.7	11.7	1.3	35.0	30.0	1.2
Case 6	273.2	200.0	1.4	12.0	9.8	1.2	33.1	29.0	1.1
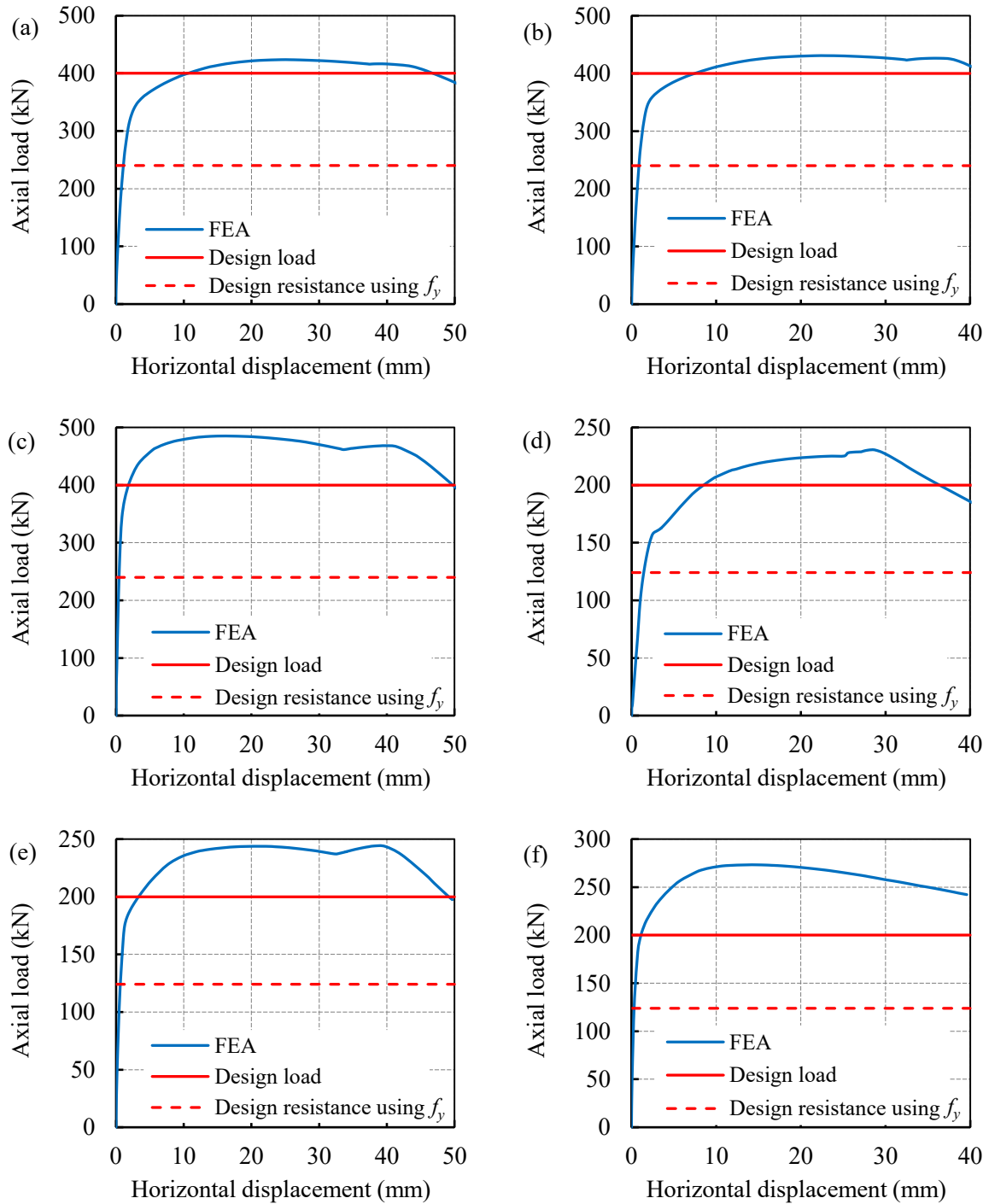
Figure 21. Comparisons between the moment-rotation curves of the FEA and the predicted strength of the joints: (a) Case 1; (b) Case 2; (c) Case 3; (d) Case 4; (e) Case 5, and (f) Case 6

8 Conclusions

In this paper, the structural behaviour and design methods of a recently proposed semi-rigid prefabricated joints for a single-layer free-form grid structure have been investigated, subjected to combined bending and compression. The proposed joint system is composed of the connected I-section beams, the front and side plates, the stiffener, the bolts, the sleeves and the central cylinder with threaded holes, which needs less labour for the onsite assembling. Design procedures and formulas are proposed to predict the load-carrying capacities of the joints theoretically. Three full-scale joints with different component dimensions are tested under the combined compression and uniaxial bending. Finite element models using ABAQUS are calibrated and validated against the tests to ensure modelling reliability. It is demonstrated that the FE model can provide good predictions against the test results in terms of the initial stiffness and ultimate capacity. Parametric studies are carried out to verify the effectiveness of the design formulas, as well as to investigate the influence of the key parameters of the components, such as the bolt distance, the thicknesses of the front plate and the side plates, the bolt diameter, the diameter of the circumcircle of the sleeves, and the thickness of the central cylinder. Through the parametric studies and verifications, it is found that:

- The load-carrying capacities of the joints increase with the increase of the front plate and the side plate thicknesses. When designing the front plate and the side plate, it is recommended to follow the proposed design formulas and assume that the front plate is simply supported. The side plate thickness is recommended to be half of the thickness of the front plate.

- The axial load-carrying capacities of the joints increase with the decrease of the bolt distances when designing in accordance with the design formulas. It is recommended to set the bolt distance to be half of the height of the front plate when designing the joints.

- The joint capacity increases with the increase of the bolt diameter and the diameter of the circumcircle of the sleeves. The bolts and the sleeves should be considered in parallel when designing the joint. The reduction of the area of the sleeves and/or the bolt diameter could result in the decrease of the joint resistance caused by the failure of the bolts.

- The central cylinders designed according to the design formulas are of sufficient strength and negligible deformations were observed in the FE analysis compared to the other components of the joints.

- The joints designed according to the proposed design formulas can be used to provide sufficient yet conservative axial load-carrying capacities and moment capacities. The design formulas can predict the deflection at the peak points of the proposed joints with reasonably good accuracy.

Acknowledgement

References

[1] Afshan S, Theofanous M, Wang J, Gkantou M, Gardner L. Testing, numerical simulation and design of prestressed high strength steel arched trusses. Engineering Structures. 2019;183:510-22.
[2] Tan Y, Zhang Y, Zhang Q, Fan F. Static properties and stability of super-long span aluminum alloy mega-latticed structures. Structures: Elsevier; 2021. p. 3173-87.
[3] Xu Y, Zhang X, Han Q. Research on the progressive collapse resistance of single-layer cylindrical latticed shells with AH joints. Thin-Walled Structures. 2021;158:107178.
[4] Han Q, Liu Y, Xu Y, Li Z. Mechanical behaviours of assembled hub joints subjected to axial loads. Journal of Constructional Steel Research. 2019;153:667-85.
[5] Han Q, Liu Y, Xu Y. Stiffness characteristics of joints and influence on the stability of single-layer latticed domes. Thin-Walled Structures. 2016;107:514-25.
[6] Liu H, Ding Y, Chen Z. Static stability behavior of aluminum alloy single-layer spherical latticed shell structure with Temcor joints. Thin-Walled Structures. 2017;120:355-65.
[7] Zhou X, He Y, Xu L. Formation and stability of a cylindrical ILTDBS reticulated mega-structure braced with single-layer latticed membranous shell substructures. Thin-walled structures. 2009;47:537-46.
[8] Ma H, Fan F, Shen S. Numerical parametric investigation of single-layer latticed domes with semi-rigid joints. Journal of the International Association for Shell and Spatial Structures. 2008;49:99-110.
[9] Ma H, Ren S, Fan F. Experimental and numerical research on a new semi-rigid joint for single-layer reticulated structures. Engineering Structures. 2016;126:725-38.
[10] Li T, Ye J, Shepherd P, Wu H, Gao B. Computational grid generation for the design of free-form shells with complex boundary conditions. Journal of Computing in Civil Engineering. 2019;33:04019004.
[11] Li Z, Ye J, Gao B, Wang Q, Quan G, Shepherd P. Digital and automatic design of free-form single-layer grid structures. Automation in Construction. 2022;133:104025.
[12] Williams C. The definition of curved geometry for widespan enclosures. Thomas Telford, London; 2000. p. 41-59.
[13] Ahmadizadeh M, Maalek S. An investigation of the effects of socket joint flexibility in space structures. Journal of Constructional Steel Research. 2014;102:72-81.
[14] Kato S, Mutoh I, Shomura M. Collapse of semi-rigidly jointed reticulated domes with initial geometric imperfections. Journal of constructional steel research. 1998;48:145-68.

[15] Han Q, Liu Y, Zhang J, Xu Y. Mechanical behaviors of the Assembled Hub (AH) joints subjected to bending moment. Journal of Constructional Steel Research. 2017;138:806-22.

[16] Ma H, Fan F, Chen G, Cao Z, Shen S. Numerical analyses of semi-rigid joints subjected to bending with and without axial force. Journal of Constructional Steel Research. 2013;90:13-28.

[17] Lopez-Arancibia A, Altuna-Zugasti A, Aldasoro HA, Pradera-Mallabiabarrena A. Bolted joints for single-layer structures: numerical analysis of the bending behaviour. Structural engineering and mechanics: An international journal. 2015;56:355-67.

[18] López A, Puente I, Serna MA. Numerical model and experimental tests on single-layer latticed domes with semi-rigid joints. Computers & structures. 2007;85:360-74.

[19] Xiang S, Cheng B, Kookalani S, Zhao J. An analytic approach to predict the shape and internal forces of barrel vault elastic gridshells during lifting construction. Structures. 2021;29:628-37.

[20] Zhang F, Du W, Zhang H. A novel bionic-based substructure division method for topology optimization. Structures. 2021;29:937-46.

[21] Tian L, Bai C, Zhong W. Experimental study and numerical simulation of partial double-layer latticed domes against progressive collapse in member-removal scenarios. Structures. 2021;29:79-91.

[22] Fathelbab F. The effect of joints on the stability of shallow single layer lattice domes: University of Cambridge; 1987.

[23] Bangash MYH, Bangash T. Elements of Spatial Structures: Analysis and Design: Thomas Telford; 2003.

[24] Zhang Y, Wang Y, Li B, Wang Z, Liu X, Zhang J et al. Structural behaviour of the aluminium alloy Temcor joints and Box-I section hybrid gusset joints under combined bending and shear. Engineering Structures. 2021;249:113380.

[25] Narayanan S. Space Structures: Principles and Practice: Multi-Science Publishing Co. Ltd; 2008.

[26] Fentiman H. Developments in Canada in the fabrication and construction of three-dimensional structures using the Triodetic system. Space Structures. 1966:1073-82.

[27] Shepherd P, Richens P. The case for subdivision surfaces in building design. Journal of the International Association for Shell and Spatial Structures. 2012;53:237-45.

[28] Muylle J, Iványi P, Topping B. A new point creation scheme for uniform Delaunay triangulation. Engineering Computations. 2002.

[29] Xu C, Wang Z, Li B, Liu Q. Form-finding and shape optimization of bio-inspired branching structures based on graphic statics. Structures: Elsevier; 2021. p. 392-407.

[30] Liew A. Constrained Force Density Method optimisation for compression-only shell structures. Structures. 2020;28:1845-56.

[31] Wang H, Chen Z, Wen G, Ji G, Xie Y. A robust node-shifting method for shape optimization of irregular gridshell structures. Structures. 2021;31:666-77.

[32] Wang Q, Ye J, Wu H, Gao B, Shepherd P. A triangular grid generation and optimization framework for the design of free-form gridshells. Computer-Aided Design. 2019;113:96-113.

[33] Gao B, Hao C, Li T, Ye J. Grid generation on free-form surface using guide line advancing and surface flattening method. Advances in Engineering Software. 2017;110:98-109.

[34] Guan Quan JQ, Hui Wu, John Ye, Boqing Gao, Nengbing Xu, Bo Hu. Experimental and numerical study on the performance of new prefaricated connections for free-form grid structures. Structures. 2022.

[35] CEN. Eurocode 1993-1-8: Eurocode 3: Design of steel structures. Part 1-8: Design of joints.: European Committee for Standarlization; 2005.

[36] GB/T 16939 High strength bolts for joints of space grid structures. 2016.

[37] GB/T 2975-1998 Steel and steel products - location and preparation of test pieces for mechanical testing 1998 [in Chinese].

[38] GB/T 1951-2018 High strength low alloy structural steels. 2018 [in Chinese].

[39] GB/T 700-2016 Hot-rolled section steel. 2016 [in Chinese].

[40] GB/T 3077-2015 Alloy structural steels. 2015 [in Chinese].

[41] GB/T 699-2015 Quality Carbon Structure Steels. 2015 [in Chinese].

[42] Yun X, Gardner L. Stress-strain curves for hot-rolled steels. Journal of Constructional Steel Research. 2017;133:36-46.

[43] Abaqus/CAE User's Manual. 2007, version 67, USA.

[44] GB/T 1951-2018 High strength low alloy structural steels. 2018 [in Chinese].

[45] GB/T 3077-2015 Alloy structural steels. 2015 [in Chinese].

[46] GB/T 699-2015 Quality Carbon Structure Steels. 2015GB/T 699-2015 Quality Carbon Structure Steels.